DESY 17-051

Investigation into the limits of perturbation theory at low Q^2 using HERA deep inelastic scattering data

I. Abt[a], A.M. Cooper-Sarkar[b], B. Foster[b,c,d], V. Myronenko[d],
K. Wichmann[d], M. Wing[e]

[a] Max-Planck-Institut für Physik, Werner-Heisenberg-Institut, München 80805, Germany

[b] Physics Department, University of Oxford, Oxford OX1 3RH, United Kingdom

[c] Hamburg University, I. Institute of Experimental Physics, Hamburg 22607, Germany

[d] Deutsches Elektronen Synchrotron DESY, Hamburg 22607, Germany

[e] Department of Physics and Astronomy, University College London, London WC1E 6BT, United Kingdom

Abstract

A phenomenological study of the final combined HERA data on inclusive deep inelastic scattering (DIS) has been performed. The data are presented and investigated for a kinematic range extending from values of the four-momentum transfer, Q^2, above $10^4\,\mathrm{GeV}^2$ down to the lowest values observable at HERA of $Q^2 = 0.045\,\mathrm{GeV}^2$ and Bjorken x, $x_{\mathrm{Bj}} = 6 \cdot 10^{-7}$. The data are well described by fits based on perturbative quantum chromodynamics (QCD) using collinear factorisation and evolution of the parton densities encompassed in the DGLAP formalism from the highest Q^2 down to Q^2 of a few GeV^2. The Regge formalism with the soft Pomeron pole can describe the data up to $Q^2 \approx 0.65\,\mathrm{GeV}^2$. The complete data set can be described by a new fit using the Abramowicz–Levin–Levy–Maor (ALLM) parameterisation. The region between the Regge and the perturbative QCD regimes is of particular interest.

1 Introduction

The HERA collider at DESY in Hamburg has provided a large amount of data on electron–proton scattering over an extensive kinematic range. Recently, the HERA collider experiments ZEUS and H1 published a combination of all inclusive deep inelastic scattering (DIS) cross sections [1].

In perturbative quantum chromodynamics (pQCD), scattering cross sections are computed by convoluting the partonic cross sections and parton density functions (PDFs), which provide the probability that a parton, either gluon or quark, with a fraction x of the proton's momentum takes part in the process. The PDFs are scale dependent, i.e. they depend on the four-momentum-transfer squared, Q^2, of the interaction. A QCD fit to the combined HERA data resulted in the family of PDFs called HERAPDF2.0 [1].

One of the surprises thrown up by HERA data has been the apparent validity of pQCD down to values of Q^2 much smaller than had been thought likely [1,2]. The QCD analysis of the final combined data, however, indicated some tension between the standard Dokshitzer–Gribov–Lipatov–Altarelli–Parisi (DGLAP) evolution [3–7] of PDFs and the cross-section data.

In recent papers [8,9], the combined data were used to investigate the necessity of higher-twist corrections to the DGLAP evolution at low values of the observable Bjorken x, $x_{\rm Bj}$, which is equal to the x of pQCD in the naive quark–parton model. The data suggest that such higher-twist corrections are needed and the resulting PDFs are uniquely suitable to investigate the validity of pQCD down to values of $Q^2 \approx 2\,{\rm GeV}^2$.

From the photoproduction regime, $Q^2 \approx 0$, to values of $Q^2 \approx 1\,{\rm GeV}^2$, pQCD can *a priori* not be applicable and models based on Regge theory [10–13] have been successfully used to describe the general features of early HERA cross-section data [14–16]. The transition from the photoproduction to the DIS regime is phenomenologically interesting, especially at very low values of $x_{\rm Bj}$. While the present paper presents an exploration of this transition region, it is not intended to be a comprehensive study of phenomenological models. Rather its purpose is to present the final HERA data in a variety of forms that have been found useful in previous theoretical analyses. These forms, both graphical and tabular, make use of a full knowledge of the correlated errors and are important input for model building in the low-Q^2 and low-$x_{\rm Bj}$ regime.

2 HERA Data, Cross Sections and Structure Functions

All HERA data on neutral current (NC) and charged current (CC) e^+p and e^-p inclusive cross sections corrected to zero beam polarisation were combined by the H1 and ZEUS collaborations to provide a coherent set of data for further analysis. The data were collected between 1994 and 2007 and represent a total integrated luminosity of $\approx 1\,{\rm fb}^{-1}$.

The investigations presented in this paper focus on the e^+p NC data, taken at centre-of-mass energies, $\sqrt{s}$, of 318 GeV and 300 GeV. Their kinematic range spans six orders of magnitude in $x_{\rm Bj}$ and Q^2, on a grid with $6.21 \cdot 10^{-7} \leq x_{\rm Bj} \leq 0.65$ and $0.045 \leq Q^2 \leq 30000\,{\rm GeV}^2$. The corresponding range of the energy available at the photon–proton vertex, $W^2 = Q^2(1/x_{\rm Bj} - 1) + m_p^2$, where m_p is the mass of the proton, is $10.7 \leq W \leq 301.2\,$GeV.

The HERA NC combined data were published as reduced cross sections, $\sigma_{r,\rm NC}$, for ep scattering. The cross-section data with $\sqrt{s} = 318\,$GeV are shown in Fig. 1 as a function of Q^2 for values of $x_{\rm Bj}$ for which more than one data point is available. For the regime of pQCD, predictions from the HHT analysis [8] at next-to-next-to-leading order (NNLO) are also shown down to a Q^2 of $2.0\,{\rm GeV}^2$. At HERA, the lowest values of $x_{\rm Bj}$ are only reached at values of Q^2 sufficiently low that pQCD is not applicable. All predictions were made from sets of PDFs which were extracted from fits to data above a minimum Q^2, which, for HHT NNLO, was $Q^2_{\rm min} = 2\,{\rm GeV}^2$. They describe the data well over their range of applicability. The predictions from the HERAPDF2.0 analysis [1] at NNLO are very similar down to $Q^2 = 3.5\,{\rm GeV}^2$, which is the $Q^2_{\rm min}$ for HERAPDF2.0.

While the regime that can be treated by pQCD is clearly limited by theoretical considerations, the data themselves show no abrupt change in behaviour in this regime. Scaling violations are well established and well described by pQCD. The slope, $d\sigma_{r,\rm NC}/dQ^2$, changes from negative to positive as $x_{\rm Bj}$ decreases. Of particular interest are $x_{\rm Bj}$ values with entries above and below $Q^2 = 1\,{\rm GeV}^2$, such as $x_{\rm Bj} = 0.0008$ and $x_{\rm Bj} = 0.0032$. The Q^2 dependence does not change in any abrupt way around $Q^2 = 1\,{\rm GeV}^2$. It seems that nature does not know about perturbation theory.

In order to describe $\sigma_{r,\rm NC}$, the generalised structure functions, $\tilde{F}_2$, $x\tilde{F}_3$ and $F_{\rm L}$, are conventionally introduced. For e^+p,

$$\sigma^{e^+p}_{r,\rm NC} = \frac{x_{\rm Bj}Q^4}{2\pi\alpha^2}\frac{1}{Y_+}\frac{d^2\sigma(e^+p)}{dx_{\rm Bj}dQ^2} = \tilde{F}_2(x_{\rm Bj},Q^2) - \frac{Y_-}{Y_+}\,x\tilde{F}_3(x_{\rm Bj},Q^2) - \frac{y^2}{Y_+}\,F_{\rm L}(x_{\rm Bj},Q^2), \qquad (1)$$

where α is the fine-structure constant and $Y_\pm = 1 \pm (1-y)^2$, with the inelasticity $y = Q^2/(s\,x_{\rm Bj})$.

The structure functions are *a priori* not limited to the perturbative regime. This limitation only arises when they are expressed in terms of parton distributions. The structure-function $\tilde{F}_2$ has components due to photon exchange, due to γZ interference and due to Z exchange. At $Q^2 \lesssim 5\,{\rm GeV}^2$, only photon exchange, described by F_2, has to be considered. As $x\tilde{F}_3$ does not have a contribution from photon exchange, it can be neglected at low Q^2.

The structure-function $F_{\rm L}$ represents the exchange of longitudinally polarised photons, while $F_2 = 2x_{\rm Bj}F_1 + F_{\rm L}$ is dominated by F_1, which describes the exchange of transversely polarised photons. For low Q^2, F_2 is dominant and Eq. 1 can be expressed as

$$\sigma^{e^+p}_{r,\rm NC} = F_2 - \frac{y^2}{Y_+}F_{\rm L} \;=\; 2x_{\rm Bj}F_1 + \frac{2(1-y)}{Y_+}\,F_{\rm L}\,. \qquad (2)$$

It has proven to be very difficult to extract $F_{\rm L}$ from HERA data. Special runs at the end of HERA operation provided data that confirmed [17,18] the expectation [19,20] that $F_{\rm L}$ is small compared to F_2 within the experimentally accessible range of $Q^2 \geq 1.5\,{\rm GeV}^2$. In order to describe data with Q^2 as low as $1.5\,{\rm GeV}^2$, a twist-four term was added to the description of $F_{\rm L}$ within the standard DGLAP formalism for the HHT analysis [8]. The resulting predictions describe the data quite well even down to $1.2\,{\rm GeV}^2$, but at such low values of Q^2, the resulting values for $F_{\rm L}$ are large and rapidly divergent and therefore unphysical.

At HERA, low x_{Bj} implies low Q^2 and vice versa. Re-expressing the factor in front of F_{L} in Eq. 2 in terms of x_{Bj} and Q^2 shows that it goes to zero proportionally to Q^2 and x_{Bj}, while F_1 is only suppressed by x_{Bj}. Thus, at HERA, the exchange of transverse photons dominates in the low-Q^2 region, independently of the exact Q^2 dependence of F_1 and F_{L}.

3 Extraction of F_2 and $\sigma^{\gamma^* p}$

Traditionally, HERA physics at low Q^2 and x_{Bj} is discussed in terms of F_2 and $\sigma^{\gamma^* p}$, defined as the cross section for virtual photon exchange. The values of F_2 have to be extracted from the reduced cross-section data. This cannot be done in an unbiased way and it cannot be done in the same way over the whole kinematic region. Indeed, on the contrary, very different models have to be used. However, in all cases, F_2 is extracted as

$$F_2^{\mathrm{extracted}} = F_2^{\mathrm{predicted}} \frac{\sigma_r^{\mathrm{measured}}}{\sigma_r^{\mathrm{predicted}}} \; . \tag{3}$$

Two different models were used to extract F_2 in two overlapping Q^2 ranges for this paper. The results of the HHT NNLO analysis [8] and Eq. 1 were used for $Q^2 \geq 1.2\,\mathrm{GeV}^2$. The contributions from γZ interference and Z exchange, which become important as Q^2 increases, were taken into account through Eq. 1. For $Q^2 \leq 2.7\,\mathrm{GeV}^2$, Eq. 2 was used to extract F_2 using estimates of $R = F_{\mathrm{L}}/(F_2 - F_{\mathrm{L}})$ from the Badelek–Kwiecinski–Stasto (BKS) model [19] for F_{L} at low x_{Bj} and low Q^2. This model is based on the kinematic constraint that $F_{\mathrm{L}} \propto Q^4$ as $Q^2 \to 0$ and on the photon–gluon fusion mechanism. The contribution of quarks having limited transverse momenta is treated phenomenologically, assuming the soft Pomeron exchange. The value of R was predicted by extrapolating F_2 to the region of low Q^2. In principle, R depends not only on Q^2, but also on x_{Bj}. However, the dependence on x_{Bj} is small and for the extraction of F_2, the average value of R over the x_{Bj} range relevant for each Q^2 value was used.

The cross section for the scattering of virtual photons on protons, $\sigma^{\gamma^* p}$, was extracted from the structure-function F_2 by using the Hand convention [21] to define the photon flux, yielding the relation [22]

$$\sigma^{\gamma^* p}(x_{\mathrm{Bj}}, Q^2) = \frac{4\pi^2\alpha(Q^2 + (2x_{\mathrm{Bj}}m_p)^2)}{Q^4(1 - x_{\mathrm{Bj}})}\, F_2(x_{\mathrm{Bj}}, Q^2) \; . \tag{4}$$

The extracted values of $\sigma^{\gamma^* p}(x_{\mathrm{Bj}}, Q^2)$ for the complete HERA data set are tabulated in Tables 1–7 and shown in Fig. 2. The values of $\sigma^{\gamma^* p}$ form a smooth plane, which again does not show any abrupt features or transitions around $Q^2 = 1\,\mathrm{GeV}^2$. For small x_{Bj}, Eq. 4 can be simplified to

$$\sigma^{\gamma^* p}(x_{\mathrm{Bj}}, Q^2) = \frac{4\pi^2\alpha}{Q^2}\, F_2(x_{\mathrm{Bj}}, Q^2) \; . \tag{5}$$

4 Features of $\sigma^{\gamma^* p}$ and Fits to F_2

The structure-function F_2 was extracted on the (x_{Bj}, Q^2)-grid given by the published ep cross-section data. The cross-section $\sigma^{\gamma^* p}$ is related to the energy available at the $\gamma^* p$ vertex, W. For low enough x_{Bj}, $W^2 = Q^2/x_{\mathrm{Bj}}$.

Figure 3 shows the complete set of extracted values of $\sigma^{\gamma^* p}$ as a function of W^2 for fixed Q^2. The BKS model was used to extract $\sigma^{\gamma^* p}$ for $Q^2 \leq 2.0\,\text{GeV}^2$ and HHT NNLO was used for $Q^2 > 2.0\,\text{GeV}^2$. As before, there is no indication of any abrupt change in behaviour around $Q^2 = 1\,\text{GeV}^2$. The cross sections rise rapidly with W for all Q^2. For high enough W, i.e. low enough x_{Bj}, a smooth power rise as $W^{2\lambda}$ is observed. As Q^2 decreases, λ also decreases.

The data can be described by fits to the Abramowicz–Levin–Levy–Maor (ALLM) parameterisation [23,24]. This *ansatz* combines Regge phenomenology with some ideas from pQCD. It describes F_2 as:

$$F_2 = \frac{Q^2}{Q^2 + m_0^2} \cdot (F_2^{I\!P} + F_2^{I\!R}) \,, \tag{6}$$

where m_0 is an effective photon mass and $F_2^{I\!P}$ and $F_2^{I\!R}$ are the contributions of Pomeron and Reggeon exchange, respectively. The parameterisation has 23 parameters, including m_0, which are associated either with Pomerons, Reggeons or mass scales. The complete set of formulae is given in the Appendix. The predictions from the ALLM97 fit [24] to early ZEUS data and the results of a new fit to the combined HERA data set called HHT-ALLM are both shown in Fig. 3.

The ALLM97 fit and the HHT-ALLM fit differ mainly due to the inclusion of high-Q^2 data, which have become available in the later years of HERA operation. This is clearly visible in Fig. 3; the ALLM97 predictions do not describe the high-Q^2 data at all. However, the description of the low-Q^2 data is also improved by the HHT-ALLM fit. The parameters of HHT-ALLM are listed and compared to the parameters of ALLM97 in Table 8. Also given are the parameters of a fit HHT-ALLM-FT, for which fixed-target data [25–27] were also included in the fit.

The HHT-ALLM fit has a good $\chi^2/\text{ndf} = 607/574 = 1.06$. Thus, the HHT-ALLM parameters were used to move points close in W to selected W values by translating them, keeping Q^2 constant. The result is shown in Fig. 4, which shows the Q^2 dependence of $\sigma^{\gamma^* p}$ for selected values of W. The measured values of $\sigma^{\gamma^* p}$ extracted with the BKS model and with the results of the HHT NNLO analysis connect smoothly at the change-over value of $Q^2 = 2.0\,\text{GeV}^2$ for all values of W. The lack of a break in this Q^2 regime is striking. However, the behaviour at high and low Q^2 differs. At high Q^2, F_2 depends only weakly on Q^2 as QCD scaling violations depend on $\ln Q^2$. Thus, $\sigma^{\gamma^* p}$ drops with $1/Q^2$ as indicated in Eq. 4 for fixed W. As $Q^2 \to 0$, the values of $\sigma^{\gamma^* p}$ have to approach the finite limit of photoproduction at $Q^2 = 0$ and F_2 has to be proportional to Q^2. The challenge is to model the smooth transition from the high- to the low-Q^2 regime. Figure 5 focuses on this region. Although generally providing a good fit, the ALLM parameterisation predicts systematically lower $\sigma^{\gamma^* p}$ values at the lowest Q^2 and highest W values.

Regge phenomenology [10] has had considerable success in parameterising the data on soft hadron–hadron collisions. In the low-Q^2 regime, the photon can be considered a hadron. Figure 5 also shows predictions from Regge fits to low-Q^2 data. At sufficiently large values of W, the total hadronic cross section is described in terms of the exchange in the t channel of a Pomeron trajectory, $\alpha_{I\!P}(t) = \alpha_{I\!P}(0) + \alpha'_{I\!P} \cdot t$. This leads to the prediction that total hadron–hadron cross sections depend on the intercept of the trajectory at $t = 0$, $\alpha_{I\!P}(0)$, as

$$\sigma^{\gamma^* p} \propto W^{2(\alpha_{I\!P}(0)-1)} \,, \tag{7}$$

where for the soft Pomeron [28] $\alpha_{I\!P}(0) \approx 1.08$. Figure 3 shows such a power-law rise for low Q^2.

At low W values, Reggeon-exchange terms also become important. The full description of F_2 in the Regge formalism [14,29] is

$$F_2(x_{\rm Bj}, Q^2) = \frac{Q^2}{4\pi^2\alpha} \cdot \frac{M_0^2}{M_0^2 + Q^2} \cdot \left(A_{I\!P} \left(\frac{Q^2}{x_{\rm Bj}}\right)^{\alpha_{I\!P}(0)-1} + A_{I\!R} \left(\frac{Q^2}{x_{\rm Bj}}\right)^{\alpha_{I\!R}(0)-1} \right), \tag{8}$$

where M_0, $A_{I\!P}$, $A_{I\!R}$, $\alpha_{I\!P}(0)$ and $\alpha_{I\!R}(0)$ are the parameters to be determined. The term $M_0^2/(M_0^2 + Q^2)$ with an effective mass M_0 arises in the framework of the generalised vector-meson dominance (GVMD) model [30,31].

New Regge fits were performed to the F_2 values as extracted from the HERA inclusive NC e^+p data with $Q^2 \le 0.65\,\text{GeV}^2$, i.e. in the regime of the so-called soft Pomeron [28]. As the W range of the HERA data for this Q^2 regime does not extend to low enough W to require a Reggeon term, the Reggeon term was omitted for the default fit. Thus, the default fit, HHT-REGGE, is a 3-parameter fit.

The predictions of the HHT-REGGE fit and of a fit previously published by the ZEUS collaboration, ZEUSREGGE [14], are shown in Fig. 5. For $Q^2 \lesssim 0.65\,\text{GeV}^2$, the Regge predictions are unsurprisingly very similar to the ALLM predictions, which are also based on Regge theory in this regime. The Regge and ALLM fits describe the overall behaviour of the data reasonably well for $Q^2 \lesssim 0.65\,\text{GeV}^2$. However, for the highest W, both fits predict $\sigma^{\gamma^* p}$ to be systematically lower than is observed. In addition, as W increases from around 50 GeV and Q^2 approaches 1 GeV^2, the Regge predictions diverge more and more from the ALLM fit.

A more detailed comparison is presented in Fig. 6, which shows the F_2 data at low Q^2 together with predictions from the HHT-REGGE and the old ZEUSREGGE fit. The data are described well by HHT-REGGE for $Q^2 \le 0.65\,\text{GeV}^2$, i.e. the fitted range.

It is expected that the simple model of a single Pomeron trajectory should start to break down beyond $Q^2 \approx 0.65\,\text{GeV}^2$ [28]. The HHT-REGGE fit has a χ^2/ndf of 0.83. Extending the fit to data with $Q^2 \le 0.85\,\text{GeV}^2$, ZEUS-REGGE-3p-.85, leads to a $\chi^2/\text{ndf} = 1.13$, confirming this expectation. Nevertheless, the data with $Q^2 \le 0.65\,\text{GeV}^2$ are still well described by the ZEUS-REGGE-3p-.85 fit. Table 9 summarises the results of all Regge fits.

If the Reggeon term is included in the HHT-REGGE fit with $A_{I\!R}$ free and $\alpha_{I\!R}(0) = 0.5$ fixed [29], the resulting HHT-REGGE-4p fit has a very good $\chi^2/\text{ndf} = 0.78$. However, $A_{I\!R}$ becomes negative with a large uncertainty. This confirms that the range in W of the HERA data alone is not sufficient to constrain the Reggeon term. The values for the Pomeron parameters are, however, consistent with the default HHT-REGGE fit. Adding the fixed-target data [25–27] does not significantly improve the constraints on the Reggeon term, see Table 9 (HHT-REGGE-FT).

The ZEUSREGGE fit was performed on low-Q^2 ($0.11 \le Q^2 \le 0.65\,\text{GeV}^2$) data on F_2 from early HERA running. This fit had $A_{I\!R}$ as a free parameter with $\alpha_{I\!R}(0) = 0.5$ fixed. This was possible because selected photoproduction data [32,33] with lower W ($6 \lesssim W \lesssim 20\,\text{GeV}$) were included in the fit.

Photoproduction data [33] were also included in a fit HHT-REGGE-PHP-5p with both $A_{I\!R}$ and $\alpha_{I\!R}(0)$ as free parameters. The inclusion of the low-W photoproduction data constrains the Reggeon term very effectively. The parameters are listed in Table 9. Figure 7 shows F_2 at low Q^2

as extracted from HERA e^+p cross sections, together with the predictions from HHT-REGGE and HHT-REGGE-PHP-5p. Within the kinematic range of the HERA data, the predictions from the two fits are basically identical. The inclusion of the fixed-target data does not improve the fit, see Table 9.

The value of the intercept $\alpha_{I\!P}(0)$ is of particular interest. The results are compatible for all HHT-REGGE fits. The value of $1.097 \pm 0.004\,(\text{stat})$ from the default fit is compatible with the old ZEUSREGGE results and with values given in the literature [29,34].

5 Characteristics of F_2

The DGLAP equations, on which the pQCD analyses are based, arise from the resummation of terms proportional to $\alpha_s^n(\ln Q^2)^m$, where α_s is the strong coupling constant and $n = m$ ($n = m-1$) at leading (next-to-leading) order. These equations do not make a prediction on the shape of the parton distributions themselves, but they describe how the parton distributions evolve with Q^2. At low x, the gluon PDF becomes dominant. The steep rise of the gluon PDF with decreasing x results in a steep rise of F_2 with decreasing x_{Bj}.

At fixed Q^2, F_2 can be parameterised as

$$F_2 = C(Q^2)x_{\text{Bj}}^{-\lambda(Q^2)}\,, \tag{9}$$

where $C(Q^2)$ and $\lambda(Q^2)$ are parameters to be fit for each Q^2. This parameterisation is inspired by QCD. At leading order (LO), the DGLAP evolution of the gluon PDF gives $xg(x, Q^2)$ proportional to $x^{-\lambda_g}$ [35] with $\lambda_g = \sqrt{12\ln(t/t_0)/(\beta_0\ln(1/x))}$, where t and t_0 are $\ln(Q^2/\Lambda^2_{\text{QCD}})$ and $\ln(Q_0^2/\Lambda^2_{\text{QCD}})$, respectively, Q_0^2 is the Q^2 at which the DGLAP evolution starts and Λ_{QCD} is the QCD scale parameter. The parameter β_0 is the QCD beta function at leading order. As $xg(x, Q^2)$ is dominant at low x, the evolution of F_2, $dF_2/d\ln(Q^2)$, is dominated by the gluon and a dependence $F_2(x, Q^2) \propto x^{-\lambda_s}$ is expected, with $\lambda_s = \lambda_g - \epsilon$, where ϵ is a small offset [35]. As a result, λ_s has an approximately logarithmic dependence on Q^2 via the $\ln(t)$ term, but it also depends on $\ln(1/x)$. Therefore, the parameterisation of Eq. 9 cannot be called a QCD prediction, but rather an approximation of LO QCD.

Regge theory suggests that $\lambda = \alpha_{I\!P}(0) - 1$ is approximately constant in the regime of soft Pomeron exchange, i.e. $Q^2 \lesssim 0.65\,\text{GeV}^2$. At higher Q^2, λ can rise. This is also called the regime of “effective Pomeron” exchange [13]. However, it is not included in the *ansatz* of Eq. 8.

The values of F_2 in each Q^2 bin were fit according to Eq. 9 for $x_{\text{Bj}} < 0.01$, i.e. in a region were valence quarks can be neglected. The four lowest-Q^2 bins were combined; as individual bins they have too few data points to produce a stable fit. The combination was achieved by translating the points from their respective Q^2 values with fixed x_{Bj} to $Q^2 = 0.11\,\text{GeV}^2$, using the predictions from the HHT-ALLM fit. The corrections to F_2 were typically around 25 %.

The values of $F_2(x_{\text{Bj}})$ and the fits are depicted in Fig. 8 for $Q^2 = 0.11$, 0.35 and 45 GeV^2. The fits are very good for all Q^2 with $\chi^2/\text{ndf} < 1$. The values for λ and C are given in Tables 10 and 11 for fits to BKS- and HHT-extracted F_2 values, respectively. The Q^2 range is considerably extended compared to values previously reported by the H1 collaboration [36]; in the common range, the values of λ and C are compatible.

Figure 9 depicts the dependence of the fit parameters λ and C on Q^2. These parameters are shown down to $Q^2 = 1.2\,\mathrm{GeV}^2$ for F_2 extracted using results from the HHT NNLO analysis, while they are shown for Q^2 up to $2.7\,\mathrm{GeV}^2$ for F_2 extracted using the BKS model[1]. The values extracted with HHT NNLO and BKS differ markedly in the overlap region. The HHT NNLO analysis implies a strong rise of λ for $Q^2 < 2.0\,\mathrm{GeV}^2$. This confirms earlier findings [8] that the HHT NNLO analysis becomes unphysical below $Q^2 = 2.0\,\mathrm{GeV}^2$, even though it can describe cross-section data in this transition region. By contrast, the extractions using the BKS model connect very smoothly to the extractions and predictions of HHT NNLO around $2\,\mathrm{GeV}^2$.

Also shown in Fig. 9 are predictions from HHT-ALLM, ALLM97, HHT-REGGE and ZEUS-REGGE. The old ALLM97 fit is based on an early subset of HERA data and cannot describe the full HERA data set. The predictions of HHT-ALLM describe the Q^2 dependence of λ and C quite well over the whole kinematic range. The large number of parameters make the ALLM parameterisation very flexible. The predictions of HHT-REGGE and ZEUSREGGE only describe the extracted values of λ and C for values of $Q^2 \lesssim 0.5\,\mathrm{GeV}^2$. The almost constant λ in this regime is the Regge soft-Pomeron explanation for the behaviour of $\sigma^{\gamma^* p}$ for low Q^2, as depicted in Fig. 3. It should be noted that the BKS model and the ALLM parameterisation are both also based on the Regge *ansatz*. Thus, the agreement between values of λ from F_2 extracted with the BKS model and the predictions from the HHT-ALLM parameterisation and the Regge fits might be an artefact. The problem in this context is that no model-independent way to extract F_2 exists. The λ values were also fitted with a first- or second-order polynomial in $\log_{10} Q^2$; for this, the HHT NNLO extraction was used for $Q^2 > 2.0\,\mathrm{GeV}^2$ and the BKS extraction for lower Q^2. The descriptions give $\chi^2/\mathrm{ndf} = 2.5$ (1.5) for the first- (second-) order polynomial.

The evolution of F_2, $dF_2/d\ln Q^2$, is an interesting quantity because, at sufficiently low values of x_{Bj}, it is connected to the gluon content of the nucleon. In pQCD, this is described by the gluon PDF. In pure Regge phenomenology, there is no concept of a gluon. However, Pomeron exchange is often interpreted as an exchange of a gluon ladder. In the alternative *ansatz* of the colour-dipole model [22], the photon splits into a $q\bar{q}$ pair which has time to evolve a complex hadronic structure through gluon radiation over a coherence length proportional to $1/Q^2$. While this scenario seems conceptually different, it is connected to the usual picture of the proton structure via a Lorentz transformation. It has been used [22] to investigate the data on $\sigma^{\gamma^* p}$ and also describes the data well.

The values of $dF_2/d\ln Q^2$ and their uncertainties were derived from fits of quadratic functions in $\ln Q^2$ to the extracted values of F_2,

$$F_2 = A(x_{\mathrm{Bj}}) + B(x_{\mathrm{Bj}}) \ln Q^2 + C(x_{\mathrm{Bj}}) \ln^2 Q^2 \,, \tag{10}$$

where A, B and C were free parameters. The values of χ^2/ndf were $\lesssim 1$ for all fits. As some values of the x_{Bj} grid had too few corresponding values on the Q^2 grid, the ALLM predictions were used to translate F_2 points along Q^2 trajectories to a reduced x_{Bj} grid. The translation factors were on the percent level.

The results on $dF_2/d\ln Q^2$ are shown in Fig. 10 as a function of x_{Bj} for selected values of Q^2. Also shown are the predictions of the HHT-ALLM and HHT-REGGE fits. The HHT-ALLM predictions follow the data quite well for Q^2 above $2\,\mathrm{GeV}^2$. At lower Q^2, neither the HHT-ALLM nor the HHT-REGGE fit agrees with the data for $x_{\mathrm{Bj}} \gtrsim 5 \cdot 10^{-5}$.

---

[1] The extraction is based on numerical results provided by the authors [19].

For $x_{\mathrm{Bj}} \geq 0.032$, the HERA data show almost perfect scaling. In this region, quarks and gluons both contribute to the evolution of F_2 but with opposite signs. The rate of scaling violation is determined by the value of $\alpha_s(Q^2)$, which is relatively small here. For $0.005 \leq x_{\mathrm{Bj}} < 0.032$, the gluon contribution becomes increasingly important and results in positive scaling violations. The range of the data in Q^2 is sufficiently wide, from $Q^2 = 2.0$ to $650\,\mathrm{GeV}^2$, to demonstrate the $\alpha_s(Q^2)$ dependence of the scaling violations. The scaling violations noticeably decrease as $\alpha_s(Q^2)$ decreases with Q^2. This is also demonstrated in Fig. 11, which shows F_2 depending on Q^2 for selected values of x_{Bj} in the regime of pQCD.

For $x_{\mathrm{Bj}} < 5 \cdot 10^{-3}$, where the $dF_2/d\ln Q^2$ values come together, the gluon contribution is dominant, leading to strong scaling violations, which increase as Q^2 increases. In this region, the range of the data in Q^2 is no longer sufficient to see any damping of this due to the dependence of $\alpha_s(Q^2)$ on Q^2.

Figure 12 shows F_2 for different values of x_{Bj} as a function of Q^2, in order to explore in more detail the region at high W (equivalent to low x_{Bj}) and low Q^2 in which disagreement between the Regge-based models and the data was observed in Fig. 5. Each plot contains data for the same four relatively high x_{Bj} values with additional data for one lower value of x_{Bj}. For the four high-x_{Bj} values repeated in each plot, the extrapolations of the HHT-REGGE and HHT-NNLO models are close and describe the data well. For the highest x_{Bj} value shown in Fig. 12 a), $x_{\mathrm{Bj}} = 2 \cdot 10^{-4}$, a gap between the extrapolations from the HHT-REGGE and HHT-NNLO models begins to be visible. Figures 12 a) – d) demonstrate how this gap grows as x_{Bj} decreases, i.e as W increases, until in Fig. 12 d) it has become substantial. Both models therefore clearly fail to describe the data in the transition region, whereas the data smoothly connect across it. Even the ALLM fit has a tendency to undershoot the data for $x_{\mathrm{Bj}} = 5 \cdot 10^{-5}$. The behaviour of the F_2 data, rising steeply in the transition region to match onto the predicted pQCD behaviour at higher Q^2, is not an artefact of the method used to extract F_2, since the behaviour is observed for F_2 values all extracted using the BKS model; the BKS model might *a priori* have been expected to favour a much shallower Regge-like behaviour. Once again, the data indicate a smooth transition between the regions in which Regge theory and pQCD give good descriptions of the data.

The derivative $dF_2/d\ln Q^2$ is shown on an enlarged scale for $x_{\mathrm{Bj}} < 10^{-2}$ in Fig. 13. The data indicate that there is a turn-over which moves to lower values of x_{Bj} as Q^2 decreases[2]. A colour-dipole inspired model introduced by Golec-Biernat and Wüsthoff (GBW) [37] predicts that a "critical line" between regimes of "soft" and "hard" scattering associated with saturation would cross the kinematic range of Fig. 13. They predict that the critical value of x_{Bj} increases with decreasing Q^2 and would be $x_{\mathrm{Bj}} \approx 2 \cdot 10^{-5}$ for $Q^2 = 2\,\mathrm{GeV}^2$ and $x_{\mathrm{Bj}} \approx 6 \cdot 10^{-4}$ at $Q^2 = 0.65\,\mathrm{GeV}^2$. However, there is no prediction on how the critical line would manifest itself. Thus, the observed lack of any transition in the behaviour of $dF_2/d\ln Q^2$ in these regions cannot confirm or exclude the GBW predictions.

6 Summary and Outlook

The combined HERA e^+p NC cross sections were studied over their complete range in x_{Bj} and Q^2, $6.21 \cdot 10^{-7} \leq x_{\mathrm{Bj}} \leq 0.65$ and $0.045 \leq Q^2 \leq 30000\,\mathrm{GeV}^2$. They were used to extract the

---

[2] At $x_{\mathrm{Bj}} = 5 \cdot 10^{-5}$, the values drop for all available Q^2. This dip is associated with a feature of the data, which is, however, of limited statistical significance.

structure-function F_2 and the photon–proton cross section $\sigma^{\gamma^* p}$. This was done by employing the pQCD analysis HHT NNLO for $Q^2 > 2.0\,\text{GeV}^2$ and a low-Q^2 approximation of the reduced cross-section together with the Regge-inspired BKS model for $Q^2 \leq 2.0\,\text{GeV}^2$. The extracted values of F_2 connect smoothly at this transition point. A new fit, HHT-REGGE, can describe the F_2 data well up to $Q^2 \leq 0.65\,\text{GeV}^2$, i.e. in the regime of the soft pomeron. The values of $\sigma^{\gamma^* p}$ derived from the F_2 data are well described by a new HHT-ALLM fit over most of the phase space, with the exception of data at the highest W, where its failure can be ascribed to the fast rise of the F_2 data between Q^2 of 1 and $2\,\text{GeV}^2$ for the lowest values of x_{Bj}.

The characteristics of F_2 were also studied by extracting λ parameters. The dependence of λ on Q^2 is reasonably well described by the HHT NNLO predictions for $Q^2 \geq 2.0\,\text{GeV}^2$ and predictions from the new HHT-REGGE fit for $Q^2 \leq 0.65\,\text{GeV}^2$. The absence of a clear transition between perturbative and non-perturbative behaviour in the data is illustrated by the fact that the extracted values of λ can also be fitted reasonably well with a second-order polynomial in $\log_{10} Q^2$.

The derivative $dF_2/d\ln Q^2$ behaves as expected for higher Q^2. For lower Q^2, it is observed that $dF_2/d\ln Q^2$ as a function of x_{Bj} shows turn-overs that move towards lower x_{Bj} as Q^2 decreases. It is unclear whether this can be ascribed to gluon saturation.

The construction of a new electron–proton or electron–ion collider [38,39] would provide more data to widen the kinematic range of future studies. In the meantime, it is hoped that the data and studies presented in this paper will catalyse theoretical work to shed further light on the transition region.

7 Acknowledgements

We would like to thank Halina Abramowicz and Aharon Levy for discussions about ALLM and Barbara Badełek and Anna Stasto for the discussions on the BKS model and their help in providing their results numerically. We would like to thank Paul Newman for discussions on Regge phenomenology. We thank our funding agencies, especially the Humboldt foundation and the MPG, for financial support and DESY for the hospitality extended to the non-DESY authors.

References

[1] H. Abramowicz *et al.* [ZEUS and H1 Collaboration], Eur. Phys. J. C **75**, 580 (2015), [arXiv:1506.06042].

[2] F. Aaron *et al.* [ZEUS and H1 Collaboration], JHEP **1001**, 109 (2010), [arXiv:0911.0884].

[3] V. Gribov and L. Lipatov, Sov. J. Nucl. Phys. **15**, 438 (1972).

[4] V. Gribov and L. Lipatov, Sov. J. Nucl. Phys. **15**, 675 (1972).

[5] L. Lipatov, Sov. J. Nucl. Phys. **20**, 94 (1975).

[6] Y. Dokshitzer, Sov. Phys. JETP **46**, 641 (1977).

[7] G. Altarelli and G. Parisi, Nucl. Phys. B **126**, 298 (1977).

[8] I. Abt *et al.* [HHT Collaboration], Phys. Rev. D **94**, 034032 (2016), [arXiv:1604.02299].

[9] L. A. Harland-Lang, A. D. Martin, P. Motylinski, and R. S. Thorne, Eur. Phys. J. C **76**, 186 (2016), [arXiv:1601.03413].

[10] P. Collins, *An Introduction to Regge Theory and High Energy Physics* (Cambridge University Press, Cambridge, UK, 1977).

[11] V. Barone and E. Predazzi, *High Energy Particle Diffraction* (in Texts and Monographs in Physics. Springer, Berlin, (2002)).

[12] A. Donnachie *et al.*, *Pomeron Physics and QCD* (Cambridge University Press, (2002)).

[13] P. Newman and M. Wing, Rev. Mod. Phys. **86**, 1037 (2014), [arXiv:1308.3368].

[14] J. Breitweg *et al.* [ZEUS Collaboration], Eur. Phys. J. C **7**, 609 (1999).

[15] J. Breitweg *et al.* [ZEUS Collaboration], Phys. Lett. B **487**, 53 (2000).

[16] C. Adloff *et al.* [H1 Collaboration], Nucl. Phys. B **497**, 3 (1997).

[17] V. Andreev *et al.* [H1 Collaboration], Eur. Phys. J. C **74**, 2814 (2014), [arXiv:1312.4821].

[18] H. Abramowicz *et al.* [ZEUS Collaboration], Phys. Rev. D **90**, 072002 (2014), [arXiv:1404.6376].

[19] B. Badelek, J. Kwiecinski and A. Stasto, Z. Phys. C **74**, 297 (1997).

[20] A. D. Martin, W. J. Stirling, and R. S. Thorne, Phys. Lett. B **635**, 305 (2006), [hep-ph/0601247].

[21] L. Hand, Phys. Rev. **129**, 1834 (1963).

[22] A. Caldwell, New. J. Phys. **18**, 073019 (2016), [arXiv:1601.04472v1].

[23] H. Abramowicz *et al.*, Phys. Lett. B **269**, 465 (1991).

[24] H. Abramowicz and A. Levy (1997), [hep-ph/9712415].

[25] M. R. Adams *et al.* [E665 Collaboration], Phys. Rev. D **54**, 3006 (1996).

[26] M. Arneodo *et al.* [New Muon Collaboration], Nucl. Phys. B **483**, 3 (1997), [hep-ph/9610231].

[27] A. C. Benvenuti *et al.* [BCDMS Collaboration], Phys. Lett. B **223**, 485 (1989).

[28] J. R. Cudell, K. Kang, and S. K. Kim, Phys. Lett. B **395**, 311 (1997), [hep-ph/9712235].

[29] A. Donnachie and P. Landshoff, Phys. Lett. B **296**, 227 (1992).

[30] J. J. Sakurai and D. Schildknecht, Phys. Lett. B **40**, 121 (1972).

[31] D. Schildknecht and H. Spiesberger (1997), [hep-ph/9707447].

[32] S. I. Alekhin *et al.* (1987), CERN-HERA 87-01.

[33] D. Caldwell *et al.*, Phys. Rev. Lett. **40**, 1222 (1978).

[34] J. R. Cudell *et al.*, Phys. Rev. D **61**, 034019 (2000), [hep-ph/9908218].

[35] A. M. Cooper-Sarkar, R. C. E. Devenish, and A. De Roeck, Int. J. Mod. Phys. A **13**, 3385 (1998), [arXiv:hep-ph/97123019].

[36] C. Adloff *et al.* [H1 Collaboration], Phys. Lett. B **520**, 183 (2001), [hep-ex:0108035].

[37] K. Golec-Biernat and M. Wüsthoff, Phys. Rev. D **59**, 014017 (1998), [hep-ph/9807513].

[38] A. Caldwell and M. Wing, Eur. Phys. J. C **76**, 463 (2016), [arXiv:1606.00783].

[39] A. Accardi *et al.*, Eur. Phys. J. A **52**, 268 (2016), [arXiv:1212.1701].

Q^2 (GeV^2)	x_{Bj}	W (GeV)	$\sigma^{\gamma^* p} \pm \delta\, \sigma^{\gamma^* p}$ (μb)	Q^2 (GeV^2)	x_{Bj}	W (GeV)	$\sigma^{\gamma^* p} \pm \delta\, \sigma^{\gamma^* p}$
0.045	6.21×10^{-7}	269.2	197.3 ± 24.1	0.35	6.62×10^{-5}	72.7	90.5 ± 3.4
0.065	8.97×10^{-7}	269.2	189.9 ± 20.6	0.35	1.30×10^{-4}	51.9	82.5 ± 2.9
0.065	1.02×10^{-6}	252.4	191.2 ± 18.7	0.35	2.20×10^{-4}	39.9	76.9 ± 3.0
0.085	1.17×10^{-6}	269.5	178.1 ± 17.1	0.35	5.00×10^{-4}	26.5	76.9 ± 2.9
0.085	1.34×10^{-6}	251.9	170.6 ± 11.6	0.35	2.51×10^{-3}	11.8	64.7 ± 7.2
0.085	1.56×10^{-6}	233.4	165.6 ± 11.8	0.4	8.83×10^{-6}	212.8	98.9 ± 5.1
0.11	1.51×10^{-6}	269.9	167.2 ± 16.4	0.4	1.10×10^{-5}	190.7	104.0 ± 3.8
0.11	1.73×10^{-6}	252.2	168.1 ± 9.5	0.4	1.33×10^{-5}	173.4	100.1 ± 3.4
0.11	2.02×10^{-6}	233.4	159.4 ± 6.4	0.4	1.70×10^{-5}	153.4	99.5 ± 2.9
0.11	2.43×10^{-6}	212.8	152.1 ± 8.5	0.4	2.20×10^{-5}	134.8	94.0 ± 2.7
0.15	2.07×10^{-6}	269.2	168.9 ± 14.2	0.4	3.68×10^{-5}	104.3	92.5 ± 3.9
0.15	2.36×10^{-6}	252.1	148.2 ± 7.2	0.4	8.83×10^{-5}	67.3	89.8 ± 3.3
0.15	2.76×10^{-6}	233.1	149.4 ± 5.4	0.4	1.76×10^{-4}	47.7	80.6 ± 3.0
0.15	3.31×10^{-6}	212.9	149.6 ± 4.9	0.4	2.94×10^{-4}	36.9	77.6 ± 3.0
0.15	4.14×10^{-6}	190.3	139.5 ± 4.7	0.4	6.31×10^{-4}	25.2	73.0 ± 3.0
0.15	5.02×10^{-6}	172.9	138.6 ± 7.8	0.5	7.32×10^{-6}	261.4	100.6 ± 10.1
0.2	3.15×10^{-6}	252.0	139.4 ± 7.2	0.5	8.60×10^{-6}	241.1	103.1 ± 11.6
0.2	3.68×10^{-6}	233.1	137.8 ± 5.2	0.5	1.58×10^{-5}	177.9	96.2 ± 4.6
0.2	4.41×10^{-6}	213.0	134.0 ± 4.2	0.5	2.12×10^{-5}	153.6	87.8 ± 2.9
0.2	5.52×10^{-6}	190.3	131.6 ± 3.8	0.5	2.76×10^{-5}	134.6	84.8 ± 2.7
0.2	6.69×10^{-6}	172.9	127.5 ± 3.4	0.5	3.98×10^{-5}	112.1	81.8 ± 3.6
0.2	8.49×10^{-6}	153.5	125.6 ± 3.8	0.5	1.00×10^{-4}	70.7	78.2 ± 2.3
0.2	1.10×10^{-5}	134.8	116.7 ± 5.1	0.5	2.51×10^{-4}	44.6	69.1 ± 2.0
0.2	3.98×10^{-5}	70.9	118.7 ± 24.5	0.5	3.68×10^{-4}	36.9	67.4 ± 2.2
0.2	2.51×10^{-4}	28.2	100.8 ± 15.5	0.5	8.00×10^{-4}	25.0	64.4 ± 2.0
0.25	3.94×10^{-6}	251.9	124.6 ± 7.3	0.5	3.20×10^{-3}	12.5	41.0 ± 5.4
0.25	4.60×10^{-6}	233.1	125.3 ± 5.1	0.65	9.52×10^{-6}	261.3	84.6 ± 5.3
0.25	5.52×10^{-6}	212.8	126.3 ± 4.1	0.65	1.12×10^{-5}	240.9	92.4 ± 5.9
0.25	6.90×10^{-6}	190.3	123.3 ± 3.6	0.65	1.58×10^{-5}	202.8	81.1 ± 5.3
0.25	8.36×10^{-6}	172.9	119.4 ± 3.5	0.65	1.64×10^{-5}	199.1	89.2 ± 7.5
0.25	1.06×10^{-5}	153.6	116.7 ± 3.1	0.65	3.98×10^{-5}	127.8	81.7 ± 3.2
0.25	1.38×10^{-5}	134.6	111.7 ± 3.1	0.65	5.98×10^{-5}	104.3	71.9 ± 3.7
0.25	2.30×10^{-5}	104.3	109.1 ± 4.3	0.65	1.00×10^{-4}	80.6	70.6 ± 2.7
0.25	3.98×10^{-5}	79.3	105.9 ± 5.0	0.65	2.51×10^{-4}	50.9	62.3 ± 2.1
0.25	1.10×10^{-4}	47.7	89.4 ± 4.5	0.65	4.78×10^{-4}	36.9	57.4 ± 2.1
0.25	2.51×10^{-4}	31.6	87.9 ± 4.6	0.65	8.00×10^{-4}	28.5	55.0 ± 1.7
0.25	3.94×10^{-4}	25.2	87.2 ± 5.2	0.65	3.20×10^{-3}	14.3	38.7 ± 2.6
0.25	1.58×10^{-3}	12.6	88.8 ± 11.2	0.85	1.24×10^{-5}	261.8	77.7 ± 3.7
0.35	5.12×10^{-6}	261.5	111.3 ± 6.4	0.85	1.38×10^{-5}	248.2	86.6 ± 11.3
0.35	5.12×10^{-6}	261.5	144.7 ± 37.2	0.85	2.00×10^{-5}	206.2	82.2 ± 3.0
0.35	6.10×10^{-6}	239.5	118.2 ± 16.7	0.85	2.00×10^{-5}	206.2	82.3 ± 4.9
0.35	6.62×10^{-6}	229.9	107.6 ± 3.7	0.85	3.98×10^{-5}	146.1	74.0 ± 2.6
0.35	8.28×10^{-6}	205.6	107.0 ± 3.4	0.85	5.00×10^{-5}	130.4	71.6 ± 4.2
0.35	1.00×10^{-5}	187.1	111.4 ± 3.2	0.85	1.00×10^{-4}	92.2	66.4 ± 4.1
0.35	1.27×10^{-5}	166.0	104.2 ± 2.9	0.85	2.51×10^{-4}	58.2	52.4 ± 3.8
0.35	1.65×10^{-5}	145.6	100.6 ± 2.8	0.85	8.00×10^{-4}	32.6	46.2 ± 2.6
0.35	3.20×10^{-5}	104.6	94.9 ± 3.9	0.85	3.20×10^{-3}	16.3	40.7 ± 2.2

Table 1: $\sigma^{\gamma^* p}(x_{\mathrm{Bj}}, Q^2)$ as extracted from the HERA e^+p NC data at $\sqrt{s} = 318$ and 300 GeV. For some values of Q^2 and x_{Bj}, two values are listed for the two different centre-of-mass energies.

Q^2 (GeV^2)	x_{Bj}	W (GeV)	$\sigma^{\gamma^* p} \pm \delta\, \sigma^{\gamma^* p}$ (μb)	Q^2 (GeV^2)	x_{Bj}	W (GeV)	$\sigma^{\gamma^* p} \pm \delta\, \sigma^{\gamma^* p}$
1.2	1.76×10^{-5}	261.1	59.6 ± 2.7	2.7	8.00×10^{-5}	183.7	37.9 ± 0.6
1.2	2.00×10^{-5}	244.9	65.8 ± 2.6	2.7	8.00×10^{-5}	183.7	38.9 ± 1.5
1.2	2.00×10^{-5}	244.9	74.3 ± 7.8	2.7	1.30×10^{-4}	144.1	33.7 ± 0.5
1.2	3.20×10^{-5}	193.6	63.6 ± 2.2	2.7	2.00×10^{-4}	116.2	32.6 ± 0.7
1.2	3.20×10^{-5}	193.6	65.2 ± 2.3	2.7	3.20×10^{-4}	91.8	29.1 ± 0.6
1.2	6.31×10^{-5}	137.9	60.9 ± 1.6	2.7	5.00×10^{-4}	73.5	26.8 ± 0.5
1.2	8.00×10^{-5}	122.5	55.7 ± 1.8	2.7	8.00×10^{-4}	58.1	24.7 ± 0.6
1.2	1.30×10^{-4}	96.1	50.8 ± 2.9	2.7	1.30×10^{-3}	45.6	23.6 ± 0.5
1.2	1.58×10^{-4}	87.1	49.8 ± 1.4	2.7	2.00×10^{-3}	36.7	20.0 ± 0.6
1.2	3.98×10^{-4}	54.9	46.1 ± 2.0	2.7	5.00×10^{-3}	23.2	18.9 ± 0.5
1.2	1.30×10^{-3}	30.4	34.8 ± 1.6	2.7	2.00×10^{-2}	11.5	14.6 ± 1.3
1.2	5.00×10^{-3}	15.5	28.0 ± 1.5	3.5	4.06×10^{-5}	293.6	32.3 ± 2.5
1.5	1.85×10^{-5}	284.5	52.3 ± 6.2	3.5	4.32×10^{-5}	284.5	34.2 ± 2.5
1.5	2.20×10^{-5}	261.4	56.4 ± 1.8	3.5	4.60×10^{-5}	275.8	36.4 ± 1.6
1.5	3.20×10^{-5}	216.5	58.2 ± 1.8	3.5	5.12×10^{-5}	261.3	34.1 ± 1.4
1.5	3.20×10^{-5}	216.5	63.8 ± 3.8	3.5	5.31×10^{-5}	256.7	31.6 ± 1.3
1.5	5.00×10^{-5}	173.2	57.5 ± 1.5	3.5	5.73×10^{-5}	247.1	36.7 ± 2.1
1.5	8.00×10^{-5}	136.9	52.5 ± 1.5	3.5	8.00×10^{-5}	209.2	31.8 ± 0.7
1.5	1.30×10^{-4}	107.4	48.4 ± 1.6	3.5	8.00×10^{-5}	209.2	33.2 ± 0.8
1.5	2.00×10^{-4}	86.6	45.8 ± 1.8	3.5	1.30×10^{-4}	164.1	29.8 ± 0.4
1.5	3.20×10^{-4}	68.5	43.2 ± 1.4	3.5	2.00×10^{-4}	132.3	27.5 ± 0.4
1.5	5.00×10^{-4}	54.8	41.0 ± 3.2	3.5	3.20×10^{-4}	104.6	25.4 ± 0.4
1.5	8.00×10^{-4}	43.3	36.7 ± 1.4	3.5	5.00×10^{-4}	83.7	24.1 ± 0.4
1.5	1.00×10^{-3}	38.7	34.6 ± 2.3	3.5	8.00×10^{-4}	66.1	21.2 ± 0.4
1.5	3.20×10^{-3}	21.6	30.8 ± 1.1	3.5	1.30×10^{-3}	51.9	20.0 ± 0.4
1.5	1.30×10^{-3}	10.7	24.6 ± 1.7	3.5	2.00×10^{-3}	41.8	18.3 ± 0.3
2	2.47×10^{-5}	284.6	50.1 ± 4.2	3.5	8.00×10^{-3}	20.9	14.9 ± 0.3
2	2.93×10^{-5}	261.4	48.3 ± 1.3	4.5	5.22×10^{-5}	293.6	28.1 ± 2.2
2	3.27×10^{-5}	247.3	52.5 ± 2.7	4.5	5.92×10^{-5}	275.7	28.2 ± 1.2
2	5.00×10^{-5}	200.0	47.3 ± 1.3	4.5	6.18×10^{-5}	269.9	27.7 ± 1.9
2	5.00×10^{-5}	200.0	49.4 ± 1.4	4.5	6.83×10^{-5}	256.7	29.9 ± 0.9
2	8.00×10^{-5}	158.1	43.1 ± 0.9	4.5	7.32×10^{-5}	247.9	27.8 ± 0.9
2	1.30×10^{-4}	124.0	40.7 ± 0.9	4.5	8.18×10^{-5}	234.5	28.8 ± 4.5
2	2.00×10^{-4}	100.0	38.1 ± 0.8	4.5	8.18×10^{-5}	234.5	30.5 ± 1.0
2	3.20×10^{-4}	79.1	35.2 ± 0.9	4.5	1.30×10^{-4}	186.0	26.0 ± 0.6
2	5.00×10^{-4}	63.2	32.3 ± 0.9	4.5	1.30×10^{-4}	186.0	26.0 ± 0.5
2	1.00×10^{-3}	44.7	28.6 ± 0.7	4.5	2.00×10^{-4}	150.0	24.2 ± 0.4
2	3.20×10^{-3}	25.0	24.0 ± 0.7	4.5	3.20×10^{-4}	118.6	22.4 ± 0.3
2	1.30×10^{-3}	12.4	20.3 ± 1.1	4.5	5.00×10^{-4}	94.8	19.9 ± 0.3
2.7	3.09×10^{-5}	295.7	46.5 ± 2.6	4.5	8.00×10^{-4}	75.0	18.0 ± 0.3
2.7	3.66×10^{-5}	271.6	43.1 ± 1.5	4.5	1.30×10^{-3}	58.8	16.6 ± 0.3
2.7	4.09×10^{-5}	256.9	44.6 ± 4.0	4.5	2.00×10^{-3}	47.4	15.4 ± 0.3
2.7	4.09×10^{-5}	256.9	47.9 ± 3.7	4.5	3.20×10^{-3}	37.5	14.3 ± 0.3
2.7	5.00×10^{-5}	232.4	39.8 ± 1.0	4.5	1.30×10^{-2}	18.5	10.9 ± 0.3
2.7	5.00×10^{-5}	232.4	41.0 ± 1.2				

Table 2: Continuation of Table 1

Q^2 (GeV^2)	$x_{\rm Bj}$	W (GeV)	$\sigma^{\gamma^* p} \pm \delta\,\sigma^{\gamma^* p}$ (μb)	Q^2 (GeV^2)	$x_{\rm Bj}$	W (GeV)	$\sigma^{\gamma^* p} \pm \delta\,\sigma^{\gamma^* p}$
6.5	7.54×10^{-5}	293.6	23.4 ± 1.8	12	1.392×10^{-4}	293.6	14.4 ± 0.5
6.5	8.03×10^{-5}	284.5	22.1 ± 1.3	12	1.61×10^{-4}	273.0	13.6 ± 0.8
6.5	8.55×10^{-5}	275.7	21.9 ± 0.9	12	1.61×10^{-4}	273.0	14.3 ± 0.3
6.5	9.52×10^{-5}	261.4	20.9 ± 0.9	12	1.82×10^{-4}	256.7	13.3 ± 0.4
6.5	9.86×10^{-5}	256.7	22.5 ± 0.7	12	2.00×10^{-4}	244.9	13.0 ± 0.3
6.5	9.86×10^{-5}	256.7	23.0 ± 1.1	12	2.00×10^{-4}	244.9	13.3 ± 0.4
6.5	1.30×10^{-4}	223.6	20.2 ± 0.4	12	3.20×10^{-4}	193.6	11.7 ± 0.2
6.5	1.30×10^{-4}	223.6	21.7 ± 0.5	12	3.20×10^{-4}	193.6	11.8 ± 0.2
6.5	2.00×10^{-4}	180.3	19.6 ± 0.3	12	5.00×10^{-4}	154.9	10.8 ± 0.1
6.5	2.00×10^{-4}	180.3	19.7 ± 0.4	12	8.00×10^{-4}	122.4	9.8 ± 0.1
6.5	3.20×10^{-4}	142.5	17.4 ± 0.2	12	1.30×10^{-3}	96.0	8.8 ± 0.1
6.5	5.00×10^{-4}	114.0	16.2 ± 0.3	12	2.00×10^{-3}	77.4	8.0 ± 0.1
6.5	8.00×10^{-4}	90.1	14.7 ± 0.2	12	3.20×10^{-3}	61.1	7.1 ± 0.1
6.5	1.30×10^{-3}	70.7	13.1 ± 0.2	12	5.00×10^{-3}	48.9	6.4 ± 0.1
6.5	2.00×10^{-3}	57.0	12.0 ± 0.2	12	2.00×10^{-2}	24.3	4.7 ± 0.1
6.5	3.20×10^{-3}	45.0	11.1 ± 0.2	15	1.74×10^{-4}	293.5	12.0 ± 0.5
6.5	5.00×10^{-3}	36.0	10.0 ± 0.2	15	2.00×10^{-4}	273.8	11.2 ± 0.6
6.5	1.30×10^{-2}	22.2	8.4 ± 0.2	15	2.00×10^{-4}	273.8	11.8 ± 0.4
6.5	2.00×10^{-2}	17.9	8.8 ± 0.3	15	2.28×10^{-4}	256.7	10.9 ± 0.3
8.5	9.86×10^{-5}	293.6	18.5 ± 0.7	15	2.46×10^{-4}	246.9	11.3 ± 0.3
8.5	1.05×10^{-4}	284.5	18.4 ± 1.1	15	3.20×10^{-4}	216.5	10.2 ± 0.2
8.5	1.12×10^{-4}	275.7	17.9 ± 0.7	15	3.20×10^{-4}	216.5	10.2 ± 0.2
8.5	1.24×10^{-4}	261.4	18.5 ± 0.6	15	5.00×10^{-4}	173.2	9.2 ± 0.1
8.5	1.29×10^{-4}	256.7	17.9 ± 0.5	15	8.00×10^{-4}	136.9	8.3 ± 0.1
8.5	1.39×10^{-4}	247.3	17.3 ± 0.9	15	1.30×10^{-3}	107.4	7.3 ± 0.1
8.5	1.39×10^{-4}	247.3	18.0 ± 1.1	15	2.00×10^{-3}	86.5	6.5 ± 0.1
8.5	2.00×10^{-4}	206.1	16.3 ± 0.3	15	3.20×10^{-3}	68.4	5.9 ± 0.1
8.5	2.00×10^{-4}	206.1	16.7 ± 0.3	15	5.00×10^{-3}	54.6	5.4 ± 0.1
8.5	3.20×10^{-4}	163.0	14.8 ± 0.2	15	8.00×10^{-3}	43.1	4.8 ± 0.1
8.5	5.00×10^{-4}	130.4	13.4 ± 0.2	15	2.00×10^{-2}	27.1	4.0 ± 0.1
8.5	8.00×10^{-4}	103.0	12.3 ± 0.2	18	2.09×10^{-4}	293.4	10.2 ± 0.4
8.5	1.30×10^{-3}	80.8	11.1 ± 0.2	18	2.37×10^{-4}	275.6	9.8 ± 0.3
8.5	2.00×10^{-3}	65.1	10.2 ± 0.2	18	2.68×10^{-4}	259.1	9.3 ± 0.5
8.5	3.20×10^{-3}	51.5	8.8 ± 0.2	18	2.68×10^{-4}	259.1	9.4 ± 0.2
8.5	5.00×10^{-3}	41.1	8.4 ± 0.2	18	3.28×10^{-4}	234.2	9.1 ± 0.2
8.5	2.00×10^{-2}	20.4	6.1 ± 0.2	18	3.28×10^{-4}	234.2	9.2 ± 0.2
10	1.30×10^{-4}	277.3	15.6 ± 1.0	18	5.00×10^{-4}	189.7	8.1 ± 0.2
10	2.00×10^{-4}	223.6	14.9 ± 0.5	18	5.00×10^{-4}	189.7	8.2 ± 0.1
10	3.20×10^{-4}	176.8	13.0 ± 0.3	18	8.00×10^{-4}	149.9	7.3 ± 0.1
10	5.00×10^{-4}	141.4	12.0 ± 0.3	18	1.30×10^{-3}	117.6	6.5 ± 0.1
10	8.00×10^{-4}	111.8	11.0 ± 0.3	18	2.00×10^{-3}	94.8	5.9 ± 0.1
10	1.30×10^{-3}	87.7	10.0 ± 0.3	18	3.20×10^{-3}	74.9	5.2 ± 0.1
10	2.00×10^{-3}	70.6	9.0 ± 0.3	18	5.00×10^{-3}	59.9	4.7 ± 0.1
10	5.00×10^{-3}	44.6	7.1 ± 0.1	18	8.00×10^{-3}	47.3	4.2 ± 0.1
10	2.00×10^{-2}	22.2	5.9 ± 0.1	18	2.00×10^{-2}	29.7	3.4 ± 0.1

Table 3: Continuation of Table 1

Q^2 (GeV^2)	$x_{\rm Bj}$	W (GeV)	$\sigma^{\gamma^* p} \pm \delta\, \sigma^{\gamma^* p}$ (μb)
22	2.90×10^{-4}	275.4	8.32 ± 0.26
22	3.20×10^{-4}	262.2	8.07 ± 0.27
22	3.45×10^{-4}	252.5	7.82 ± 0.18
22	3.88×10^{-4}	238.1	7.56 ± 0.15
22	5.00×10^{-4}	209.7	7.12 ± 0.25
22	5.00×10^{-4}	209.7	7.29 ± 0.14
22	5.92×10^{-4}	192.7	6.92 ± 0.13
22	8.00×10^{-4}	165.8	6.34 ± 0.10
22	1.30×10^{-3}	130.0	5.42 ± 0.16
22	2.00×10^{-3}	104.8	5.07 ± 0.11
22	3.20×10^{-3}	82.8	4.61 ± 0.14
22	5.00×10^{-3}	66.2	3.94 ± 0.11
22	8.00×10^{-3}	52.2	3.37 ± 0.10
22	1.30×10^{-2}	40.9	3.03 ± 0.09
22	3.20×10^{-2}	25.8	2.74 ± 0.08
27	3.14×10^{-4}	293.2	7.30 ± 0.35
27	3.35×10^{-4}	283.9	7.00 ± 0.41
27	3.55×10^{-4}	275.7	6.79 ± 0.20
27	4.10×10^{-4}	256.6	6.56 ± 0.19
27	4.10×10^{-4}	256.6	6.63 ± 0.17
27	5.00×10^{-4}	232.3	6.19 ± 0.10
27	5.00×10^{-4}	232.3	6.28 ± 0.15
27	8.00×10^{-4}	183.6	5.45 ± 0.07
27	8.00×10^{-4}	183.6	5.47 ± 0.16
27	1.30×10^{-3}	144.0	4.83 ± 0.06
27	2.00×10^{-3}	116.1	4.36 ± 0.05
27	3.20×10^{-3}	91.7	3.81 ± 0.05
27	5.00×10^{-3}	73.3	3.34 ± 0.04
27	8.00×10^{-3}	57.9	2.96 ± 0.04
27	1.30×10^{-2}	45.3	2.67 ± 0.04
27	2.00×10^{-2}	36.4	2.44 ± 0.04
27	3.20×10^{-2}	28.6	2.26 ± 0.06
35	4.60×10^{-4}	275.7	5.17 ± 0.13
35	5.00×10^{-4}	264.5	5.21 ± 0.14
35	5.31×10^{-4}	256.6	5.03 ± 0.09
35	5.74×10^{-4}	246.9	5.30 ± 0.15
35	6.16×10^{-4}	238.3	4.96 ± 0.10
35	6.57×10^{-4}	230.7	4.83 ± 0.09
35	8.00×10^{-4}	209.1	4.59 ± 0.06
35	8.00×10^{-4}	209.1	4.67 ± 0.09
35	1.00×10^{-3}	187.0	4.28 ± 0.07
35	1.30×10^{-3}	164.0	3.96 ± 0.05
35	2.00×10^{-3}	132.2	3.54 ± 0.04
35	3.20×10^{-3}	104.4	3.10 ± 0.04
35	5.00×10^{-3}	83.5	2.74 ± 0.03
35	8.00×10^{-3}	65.9	2.41 ± 0.03
35	1.30×10^{-2}	51.6	2.15 ± 0.03
35	2.00×10^{-2}	41.4	1.93 ± 0.03
35	3.20×10^{-2}	32.6	1.71 ± 0.03
35	8.00×10^{-2}	20.1	1.56 ± 0.08
45	5.90×10^{-4}	276.1	4.12 ± 0.15
45	6.34×10^{-4}	266.3	4.00 ± 0.09
45	7.00×10^{-4}	253.5	4.00 ± 0.11
45	8.00×10^{-4}	237.1	3.85 ± 0.06
45	8.00×10^{-4}	237.1	3.99 ± 0.13
45	9.20×10^{-4}	221.1	3.60 ± 0.07
45	1.10×10^{-3}	202.2	3.51 ± 0.06
45	1.30×10^{-3}	185.9	3.29 ± 0.04
45	1.30×10^{-3}	185.9	3.33 ± 0.05
45	2.00×10^{-3}	149.9	2.90 ± 0.03
45	3.20×10^{-3}	118.4	2.52 ± 0.03
45	5.00×10^{-3}	94.6	2.25 ± 0.03
45	8.00×10^{-3}	74.7	1.96 ± 0.02
45	1.30×10^{-2}	58.5	1.72 ± 0.02
45	2.00×10^{-2}	47.0	1.53 ± 0.02
45	3.20×10^{-2}	36.9	1.37 ± 0.02
45	5.00×10^{-2}	29.3	1.27 ± 0.03
60	8.00×10^{-4}	273.8	3.07 ± 0.06
60	8.60×10^{-4}	264.0	3.17 ± 0.10
60	9.40×10^{-4}	252.5	3.07 ± 0.10
60	1.10×10^{-3}	233.4	2.87 ± 0.07
60	1.30×10^{-3}	214.7	2.69 ± 0.04
60	1.30×10^{-3}	214.7	2.73 ± 0.06
60	1.50×10^{-3}	199.9	2.52 ± 0.05
60	2.00×10^{-3}	173.0	2.34 ± 0.03
60	3.20×10^{-3}	136.7	2.03 ± 0.02
60	5.00×10^{-3}	109.3	1.75 ± 0.02
60	8.00×10^{-3}	86.3	1.54 ± 0.02
60	1.30×10^{-2}	67.5	1.34 ± 0.02
60	2.00×10^{-2}	54.2	1.20 ± 0.02
60	3.20×10^{-2}	42.6	1.07 ± 0.02
60	5.00×10^{-2}	33.8	1.00 ± 0.02
60	1.30×10^{-1}	20.1	0.85 ± 0.05

Table 4: Continuation of Table 1

Q^2 (GeV^2)	x_{Bj}	W (GeV)	$\sigma^{\gamma^* p} \pm \delta\, \sigma^{\gamma^* p}$ (μb)	Q^2 (GeV^2)	x_{Bj}	W (GeV)	$\sigma^{\gamma^* p} \pm \delta\, \sigma^{\gamma^* p}$
70	$9.22{\times}10^{-4}$	275.4	2.481 ± 0.158	120	$5.00{\times}10^{-2}$	47.8	0.478 ± 0.009
70	$1.00{\times}10^{-3}$	264.4	2.516 ± 0.091	120	$8.00{\times}10^{-2}$	37.2	0.448 ± 0.009
70	$1.10{\times}10^{-3}$	252.1	2.593 ± 0.081	120	$1.80{\times}10^{-1}$	23.4	0.379 ± 0.015
70	$1.24{\times}10^{-3}$	237.4	2.442 ± 0.065	150	$2.00{\times}10^{-3}$	273.6	1.138 ± 0.022
70	$1.30{\times}10^{-3}$	231.9	2.377 ± 0.056	150	$3.20{\times}10^{-3}$	216.2	0.937 ± 0.023
70	$1.30{\times}10^{-3}$	231.9	2.463 ± 0.061	150	$3.20{\times}10^{-3}$	216.2	0.953 ± 0.013
70	$2.00{\times}10^{-3}$	186.9	2.033 ± 0.044	150	$5.00{\times}10^{-3}$	172.8	0.818 ± 0.010
70	$2.00{\times}10^{-3}$	186.9	2.070 ± 0.043	150	$8.00{\times}10^{-3}$	136.4	0.701 ± 0.011
70	$2.50{\times}10^{-3}$	167.1	1.930 ± 0.035	150	$1.30{\times}10^{-2}$	106.7	0.605 ± 0.012
70	$3.20{\times}10^{-3}$	147.7	1.752 ± 0.027	150	$2.00{\times}10^{-2}$	85.7	0.524 ± 0.011
70	$5.00{\times}10^{-3}$	118.0	1.546 ± 0.023	150	$3.20{\times}10^{-2}$	67.4	0.451 ± 0.011
70	$8.00{\times}10^{-3}$	93.2	1.325 ± 0.025	150	$5.00{\times}10^{-2}$	53.4	0.401 ± 0.009
70	$1.30{\times}10^{-2}$	72.9	1.163 ± 0.026	150	$8.00{\times}10^{-2}$	41.5	0.360 ± 0.008
70	$2.00{\times}10^{-2}$	58.6	1.041 ± 0.022	150	$1.80{\times}10^{-1}$	26.2	0.296 ± 0.011
70	$3.20{\times}10^{-2}$	46.0	0.929 ± 0.023	200	$2.60{\times}10^{-3}$	277.0	0.813 ± 0.017
70	$5.00{\times}10^{-2}$	36.5	0.863 ± 0.020	200	$3.20{\times}10^{-3}$	249.6	0.710 ± 0.034
90	$1.30{\times}10^{-3}$	262.9	2.007 ± 0.038	200	$3.20{\times}10^{-3}$	249.6	0.743 ± 0.013
90	$1.50{\times}10^{-3}$	244.8	1.876 ± 0.048	200	$5.00{\times}10^{-3}$	199.5	0.619 ± 0.015
90	$2.00{\times}10^{-3}$	211.9	1.623 ± 0.041	200	$5.00{\times}10^{-3}$	199.5	0.637 ± 0.007
90	$2.00{\times}10^{-3}$	211.9	1.706 ± 0.027	200	$8.00{\times}10^{-3}$	157.5	0.539 ± 0.006
90	$3.20{\times}10^{-3}$	167.4	1.470 ± 0.019	200	$1.30{\times}10^{-2}$	123.2	0.460 ± 0.005
90	$5.00{\times}10^{-3}$	133.8	1.286 ± 0.016	200	$2.00{\times}10^{-2}$	99.0	0.401 ± 0.004
90	$8.00{\times}10^{-3}$	105.6	1.110 ± 0.015	200	$3.20{\times}10^{-2}$	77.8	0.337 ± 0.004
90	$1.30{\times}10^{-2}$	82.7	0.952 ± 0.014	200	$5.00{\times}10^{-2}$	61.7	0.307 ± 0.004
90	$2.00{\times}10^{-2}$	66.4	0.826 ± 0.012	200	$8.00{\times}10^{-2}$	48.0	0.267 ± 0.003
90	$3.20{\times}10^{-2}$	52.2	0.717 ± 0.011	200	$1.30{\times}10^{-1}$	36.6	0.233 ± 0.006
90	$5.00{\times}10^{-2}$	41.4	0.641 ± 0.012	200	$1.80{\times}10^{-1}$	30.2	0.234 ± 0.004
90	$8.00{\times}10^{-2}$	32.2	0.591 ± 0.011	200	$2.50{\times}10^{-1}$	24.5	0.208 ± 0.012
90	$1.80{\times}10^{-1}$	20.3	0.522 ± 0.027	200	$4.00{\times}10^{-1}$	17.3	0.131 ± 0.010
120	$1.60{\times}10^{-3}$	273.6	1.457 ± 0.027	250	$3.30{\times}10^{-3}$	274.8	0.630 ± 0.014
120	$1.72{\times}10^{-3}$	263.9	1.468 ± 0.062	250	$5.00{\times}10^{-3}$	223.0	0.506 ± 0.016
120	$1.88{\times}10^{-3}$	252.4	1.412 ± 0.052	250	$5.00{\times}10^{-3}$	223.0	0.524 ± 0.007
120	$2.00{\times}10^{-3}$	244.7	1.348 ± 0.023	250	$8.00{\times}10^{-3}$	176.1	0.434 ± 0.005
120	$2.12{\times}10^{-3}$	237.7	1.322 ± 0.039	250	$1.30{\times}10^{-2}$	137.8	0.377 ± 0.004
120	$2.12{\times}10^{-3}$	237.7	1.362 ± 0.042	250	$2.00{\times}10^{-2}$	110.7	0.324 ± 0.004
120	$2.70{\times}10^{-3}$	210.5	1.199 ± 0.036	250	$3.20{\times}10^{-2}$	87.0	0.274 ± 0.003
120	$3.20{\times}10^{-3}$	193.3	1.130 ± 0.027	250	$5.00{\times}10^{-2}$	68.9	0.245 ± 0.003
120	$3.20{\times}10^{-3}$	193.3	1.153 ± 0.014	250	$8.00{\times}10^{-2}$	53.6	0.215 ± 0.003
120	$5.00{\times}10^{-3}$	154.5	0.984 ± 0.014	250	$1.30{\times}10^{-1}$	40.9	0.189 ± 0.004
120	$8.00{\times}10^{-3}$	122.0	0.843 ± 0.012	250	$1.80{\times}10^{-1}$	33.8	0.181 ± 0.003
120	$1.30{\times}10^{-2}$	95.5	0.733 ± 0.012	250	$2.50{\times}10^{-1}$	27.4	0.160 ± 0.007
120	$2.00{\times}10^{-2}$	76.7	0.635 ± 0.011	250	$4.00{\times}10^{-1}$	19.4	0.106 ± 0.007
120	$3.20{\times}10^{-2}$	60.3	0.554 ± 0.010				

Table 5: Continuation of Table 1

Q^2 (GeV^2)	x_{Bj}	W (GeV)	$\sigma^{\gamma^* p} \pm \delta\, \sigma^{\gamma^* p}$ (μb)	Q^2 (GeV^2)	x_{Bj}	W (GeV)	$\sigma^{\gamma^* p} \pm \delta\, \sigma^{\gamma^* p}$
300	0.0039	276.8	0.500 ± 0.011	650	0.032	140.2	0.112 ± 0.002
300	0.005	244.3	0.450 ± 0.008	650	0.05	111.1	0.094 ± 0.001
300	0.005	244.3	0.451 ± 0.019	650	0.08	86.5	0.082 ± 0.001
300	0.008	192.9	0.370 ± 0.004	650	0.13	66.0	0.072 ± 0.001
300	0.008	192.9	0.375 ± 0.011	650	0.18	54.4	0.070 ± 0.002
300	0.013	150.9	0.309 ± 0.003	650	0.25	44.2	0.057 ± 0.001
300	0.02	121.2	0.268 ± 0.003	650	0.4	31.2	0.042 ± 0.002
300	0.032	95.3	0.231 ± 0.003	650	0.65	18.7	0.011 ± 0.002
300	0.05	75.5	0.199 ± 0.003	800	0.0105	274.6	0.142 ± 0.004
300	0.08	58.7	0.176 ± 0.002	800	0.013	246.5	0.125 ± 0.002
300	0.13	44.8	0.159 ± 0.003	800	0.013	246.5	0.133 ± 0.005
300	0.18	37.0	0.149 ± 0.002	800	0.02	198.0	0.106 ± 0.002
300	0.25	30.0	0.134 ± 0.007	800	0.02	198.0	0.107 ± 0.005
300	0.4	21.2	0.099 ± 0.004	800	0.032	155.6	0.091 ± 0.001
400	0.0053	274.0	0.361 ± 0.008	800	0.05	123.3	0.077 ± 0.001
400	0.008	222.7	0.280 ± 0.009	800	0.08	95.9	0.070 ± 0.001
400	0.008	222.7	0.296 ± 0.004	800	0.13	73.2	0.058 ± 0.001
400	0.013	174.3	0.241 ± 0.003	800	0.18	60.4	0.056 ± 0.002
400	0.013	174.3	0.245 ± 0.008	800	0.25	49.0	0.047 ± 0.001
400	0.02	140.0	0.205 ± 0.003	800	0.4	34.7	0.031 ± 0.002
400	0.032	110.0	0.174 ± 0.002	800	0.65	20.8	0.008 ± 0.001
400	0.05	87.2	0.151 ± 0.002	1000	0.013	275.5	0.100 ± 0.003
400	0.08	67.8	0.133 ± 0.002	1000	0.02	221.4	0.086 ± 0.002
400	0.13	51.7	0.118 ± 0.002	1000	0.02	221.4	0.087 ± 0.006
400	0.18	42.7	0.109 ± 0.004	1000	0.032	173.9	0.073 ± 0.002
400	0.25	34.7	0.098 ± 0.002	1000	0.05	137.8	0.063 ± 0.002
400	0.4	24.5	0.075 ± 0.003	1000	0.08	107.2	0.054 ± 0.001
500	0.0066	274.3	0.256 ± 0.006	1000	0.13	81.8	0.047 ± 0.001
500	0.008	249.0	0.236 ± 0.005	1000	0.18	67.5	0.043 ± 0.001
500	0.008	249.0	0.246 ± 0.016	1000	0.25	54.8	0.038 ± 0.001
500	0.013	194.8	0.201 ± 0.003	1000	0.4	38.7	0.025 ± 0.001
500	0.013	194.8	0.205 ± 0.013	1000	0.65	23.2	0.006 ± 0.001
500	0.02	156.5	0.170 ± 0.003	1200	0.014	290.7	0.086 ± 0.002
500	0.032	123.0	0.144 ± 0.002	1200	0.014	290.7	0.093 ± 0.006
500	0.05	97.5	0.126 ± 0.002	1200	0.02	242.5	0.070 ± 0.003
500	0.08	75.8	0.108 ± 0.002	1200	0.02	242.5	0.075 ± 0.001
500	0.13	57.9	0.097 ± 0.002	1200	0.032	190.5	0.058 ± 0.002
500	0.18	47.7	0.085 ± 0.002	1200	0.032	190.5	0.062 ± 0.001
500	0.25	38.7	0.078 ± 0.003	1200	0.05	151.0	0.051 ± 0.001
500	0.4	27.4	0.064 ± 0.006	1200	0.08	117.5	0.045 ± 0.001
650	0.0085	275.4	0.177 ± 0.010	1200	0.13	89.6	0.039 ± 0.001
650	0.0085	275.4	0.187 ± 0.005	1200	0.18	73.9	0.037 ± 0.001
650	0.013	222.2	0.152 ± 0.005	1200	0.25	60.0	0.031 ± 0.001
650	0.013	222.2	0.154 ± 0.002	1200	0.4	42.4	0.020 ± 0.001
650	0.02	178.5	0.125 ± 0.007	1200	0.65	25.4	0.006 ± 0.001
650	0.02	178.5	0.132 ± 0.002				

Table 6: Continuation of Table 1

Q^2 (GeV^2)	$x_{\rm Bj}$	W (GeV)	$\sigma^{\gamma^* p} \pm \delta\, \sigma^{\gamma^* p}$ (μb)	Q^2 (GeV^2)	$x_{\rm Bj}$	W (GeV)	$\sigma^{\gamma^* p} \pm \delta\, \sigma^{\gamma^* p}$
1500	0.02	271.1	0.0576 ± 0.0016	5000	0.0547	294.0	0.0132 ± 0.0008
1500	0.02	271.1	0.0608 ± 0.0044	5000	0.08	239.8	0.0102 ± 0.0007
1500	0.032	213.0	0.0443 ± 0.0031	5000	0.08	239.8	0.0114 ± 0.0003
1500	0.032	213.0	0.0476 ± 0.0011	5000	0.13	182.9	0.0093 ± 0.0008
1500	0.05	168.8	0.0432 ± 0.0008	5000	0.13	182.9	0.0094 ± 0.0003
1500	0.08	131.3	0.0369 ± 0.0007	5000	0.18	150.9	0.0080 ± 0.0003
1500	0.13	100.2	0.0304 ± 0.0007	5000	0.25	122.5	0.0068 ± 0.0003
1500	0.18	82.7	0.0284 ± 0.0007	5000	0.4	86.6	0.0044 ± 0.0002
1500	0.25	67.1	0.0246 ± 0.0007	5000	0.65	51.9	0.0007 ± 0.0001
1500	0.4	47.4	0.0156 ± 0.0006	8000	0.0875	288.8	0.0071 ± 0.0007
1500	0.65	28.4	0.0033 ± 0.0004	8000	0.13	231.4	0.0053 ± 0.0006
2000	0.0219	298.9	0.0448 ± 0.0029	8000	0.13	231.4	0.0061 ± 0.0002
2000	0.032	246.0	0.0358 ± 0.0010	8000	0.18	190.9	0.0052 ± 0.0002
2000	0.032	246.0	0.0367 ± 0.0024	8000	0.18	190.9	0.0056 ± 0.0006
2000	0.05	194.9	0.0301 ± 0.0018	8000	0.25	154.9	0.0043 ± 0.0002
2000	0.05	194.9	0.0311 ± 0.0008	8000	0.25	154.9	0.0047 ± 0.0006
2000	0.08	151.7	0.0276 ± 0.0006	8000	0.4	109.5	0.0024 ± 0.0002
2000	0.13	115.7	0.0234 ± 0.0006	8000	0.65	65.6	0.0006 ± 0.0001
2000	0.18	95.5	0.0204 ± 0.0006	12000	0.13	283.4	0.0034 ± 0.0007
2000	0.25	77.5	0.0181 ± 0.0006	12000	0.18	233.8	0.0035 ± 0.0006
2000	0.4	54.8	0.0119 ± 0.0005	12000	0.18	233.8	0.0036 ± 0.0002
2000	0.65	32.8	0.0027 ± 0.0003	12000	0.25	189.7	0.0024 ± 0.0002
3000	0.032	301.2	0.0260 ± 0.0011	12000	0.25	189.7	0.0024 ± 0.0005
3000	0.05	238.7	0.0217 ± 0.0005	12000	0.4	134.2	0.0016 ± 0.0001
3000	0.05	238.7	0.0223 ± 0.0014	12000	0.65	80.4	0.0004 ± 0.0001
3000	0.08	185.7	0.0182 ± 0.0005	20000	0.25	245.0	0.0017 ± 0.0002
3000	0.08	185.7	0.0188 ± 0.0012	20000	0.25	245.0	0.0020 ± 0.0006
3000	0.13	141.7	0.0153 ± 0.0004	20000	0.4	173.2	0.0010 ± 0.0002
3000	0.18	116.9	0.0136 ± 0.0004	20000	0.4	173.2	0.0015 ± 0.0005
3000	0.25	94.9	0.0114 ± 0.0004	20000	0.65	103.8	0.0002 ± 0.0001
3000	0.4	67.1	0.0076 ± 0.0003	30000	0.4	212.1	0.0007 ± 0.0002
3000	0.65	40.2	0.0016 ± 0.0002	30000	0.4	212.1	0.0016 ± 0.0010
				30000	0.65	127.1	0.0001 ± 0.0001

Table 7: Continuation of Table 1

parameter	HHT-ALLM	HHT-ALLM-FT	ALLM-97
m_0	0.446 ± 0.028	0.388 ± 0.021	0.320
p_1	74.2 ± 17.5	50.8 ± 10.3	49.5
p_2	29.3 ± 13.6	0.838 ± 0.273	0.151
p_3	$4.74\times10^{-5} \pm 2.63 \times 10^{-5}$	$1.87 \times 10^{-5} \pm 5 \times 10^{-7}$	0.525
p_4	$2.2\times10^{-8} \pm 1.7 \times 10^{-8}$	$4.4 \times 10^{-9} \pm 4 \times 10^{-10}$	0.065
p_5	0.412 ± 0.018	0.356 ± 0.013	0.281
p_6	0.164 ± 0.011	0.171 ± 0.005	0.223
p_7	17.7 ± 1.1	18.6 ± 0.8	2.20
p_8	−0.835 ± 0.007	−0.075 ± 0.007	−0.081
p_9	−0.446 ± 0.022	−0.470 ± 0.014	−0.448
p_{10}	10.6 ± 1.2	9.2 ± 0.5	1.17
p_{11}	−45.8 ± 1.0	−0.477 ± 0.329	0.363
p_{12}	55.7 ± 1.0	54.0 ± 0.4	1.89
p_{13}	−0.031 ± 0.152	0.073 ± 0.068	1.84
p_{14}	−1.04 ± 0.13	−0.636 ± 0.033	0.801
p_{15}	2.97 ± 0.13	3.37 ± 0.03	0.97
p_{16}	0.163 ± 0.044	−0.660 ± 0.254	3.49
p_{17}	0.706 ± 0.081	0.882 ± 0.042	0.584
p_{18}	0.185 ± 0.085	0.082 ± 0.0279	0.379
p_{19}	−16.4 ± 2.6	−8.5 ± 1.6	2.61
p_{20}	−1.29 ± 1.32	0.339 ± 0.021	0.011
p_{21}	4.51 ± 1.30	3.38 ± 0.02	3.76
p_{22}	1.16 ± 0.39	1.07 ± 0.10	0.493
χ^2/ndf	607/574=1.06	1014/1001=1.01	1299/1357=0.97

Table 8: Parameters of the HHT-ALLM fit to HERA data only, compared to parameters obtained when adding fixed-target data [25–27] to the fit, HHT-ALLM-FT. The parameter values of the ALLM97 fit published previously [24], using early HERA and other data, are also listed. The formulae for the ALLM parameterisation are provided in the Appendix; the units can be deduced from these formulae.

Name	Fit Parameters					χ^2/
of Fit	M_0^2 (GeV^2)	$A_{I\!P}$ (μb)	$\alpha_{I\!P}(0)$	$A_{I\!R}$ (μb)	$\alpha_{I\!R}(0)$	ndf
HHT-REGGE	0.50 ±0.03	66.3 ± 3.2	1.097 ± 0.004	fixed to 0	–	0.83
3p-.85	0.58 ±0.03	58.5 ± 2.5	1.105 ± 0.003	fixed to 0	–	1.13
4p	0.49 ±0.03	78.5 ± 7.1	1.082 ± 0.008	−230 ±105	fixed to 0.5	0.78
FT-4p	0.50 ±0.02	77.4 ± 5.6	1.083 ± 0.006	−217 ± 60	fixed to 0.5	0.75
PHP-5p	0.52 ±0.01	57.0 ± 4.7	1.110 ± 0.007	193 ± 51	0.50 ±0.11	1.16
PHP-FT-5p	0.48 ±0.01	58.9 ± 3.0	1.110 ± 0.005	263 ± 69	0.39 ±0.09	1.35
ZEUSREGGE	fixed to 0.53	63.5 ± 0.9	1.097 ± 0.002	145 ± 2	fixed to 0.5	1.12
update	0.52 ± 0.04	62.0 ± 2.3	1.102 ± 0.007	148 ± 5	fixed to 0.5	–

Table 9: Summary of the results of the HHT-REGGE fits, for details see text. Also listed are results previously published as ZEUSREGGE [14]. The HERA data at that time were not yet sufficient to constrain M_0 in the fit. Therefore, M_0 was extracted from the data within the framework of the GVMD model [30,31] to be $M_0^2 = 0.53 \pm 0.04(stat) \pm 0.09(syst)$ GeV^2 and fixed to 0.53 in the ZEUSREGGE fit. An update [15] to the ZEUSREGGE fit was published including more early ZEUS data, allowing M_0 to be a free parameter. This update provided compatible results but slightly larger uncertainties and no χ^2 was provided. Therefore, the parameters of the original ZEUSREGGE fit were used for all comparisons throughout this paper.

Q^2 (GeV^2)	λ	C
0.11	0.171 ± 0.033	0.017 ± 0.007
0.20	0.102 ± 0.029	0.068 ± 0.024
0.25	0.089 ± 0.009	0.094 ± 0.010
0.35	0.092 ± 0.007	0.115 ± 0.009
0.40	0.080 ± 0.008	0.145 ± 0.013
0.50	0.100 ± 0.008	0.136 ± 0.010
0.65	0.125 ± 0.008	0.126 ± 0.009
0.85	0.137 ± 0.010	0.137 ± 0.013
1.20	0.150 ± 0.008	0.144 ± 0.010
1.50	0.135 ± 0.007	0.192 ± 0.012
2.00	0.161 ± 0.006	0.171 ± 0.009
2.70	0.168 ± 0.005	0.182 ± 0.007

Table 10: The fitted values of λ and C from Eq. 9 for F_2 extracted with the BKS model.

Q^2 (GeV^2)	λ	C
1.2	0.230 ± 0.010	0.076 ± 0.007
1.5	0.179 ± 0.007	0.138 ± 0.009
2.0	0.178 ± 0.006	0.149 ± 0.008
2.7	0.176 ± 0.005	0.171 ± 0.007
3.5	0.172 ± 0.004	0.198 ± 0.006
4.5	0.191 ± 0.005	0.189 ± 0.007
6.5	0.202 ± 0.004	0.199 ± 0.006
8.5	0.213 ± 0.005	0.202 ± 0.007
10	0.225 ± 0.008	0.193 ± 0.011
12	0.223 ± 0.005	0.211 ± 0.008
15	0.241 ± 0.004	0.197 ± 0.005
18	0.245 ± 0.004	0.204 ± 0.005
22	0.263 ± 0.007	0.191 ± 0.009
27	0.270 ± 0.004	0.193 ± 0.006
35	0.281 ± 0.005	0.192 ± 0.006
45	0.293 ± 0.005	0.189 ± 0.006
60	0.314 ± 0.007	0.178 ± 0.007
70	0.328 ± 0.010	0.168 ± 0.010
90	0.317 ± 0.010	0.190 ± 0.011
120	0.348 ± 0.011	0.166 ± 0.010
150	0.349 ± 0.016	0.172 ± 0.015
200	0.360 ± 0.017	0.167 ± 0.015
250	0.414 ± 0.025	0.130 ± 0.017
300	0.419 ± 0.030	0.130 ± 0.020

Table 11: The fitted values of λ and C from Eq. 9 for F_2 extracted with results from the HHT NNLO analysis.

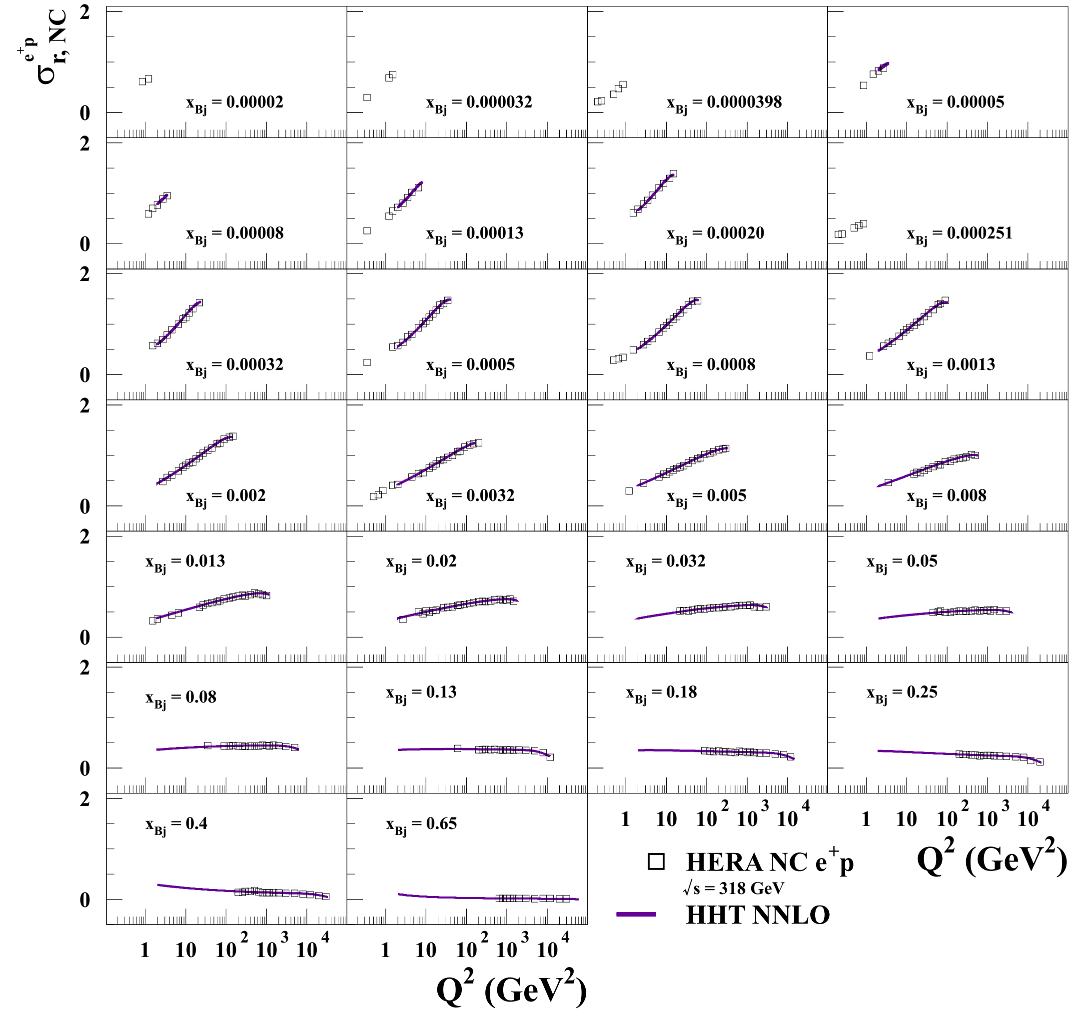

Figure 1: The combined HERA data on the inclusive NC e^+p reduced cross sections with $\sqrt{s}$ = 318 GeV as a function of Q^2 for 26 selected bins of x_{Bj}. Also shown are the predictions from the HHT NNLO [8] analysis down to Q^2 = 2.0 GeV^2. The width of the bands represents the uncertainty on the predictions. The errors bars on the data are smaller than the symbols.

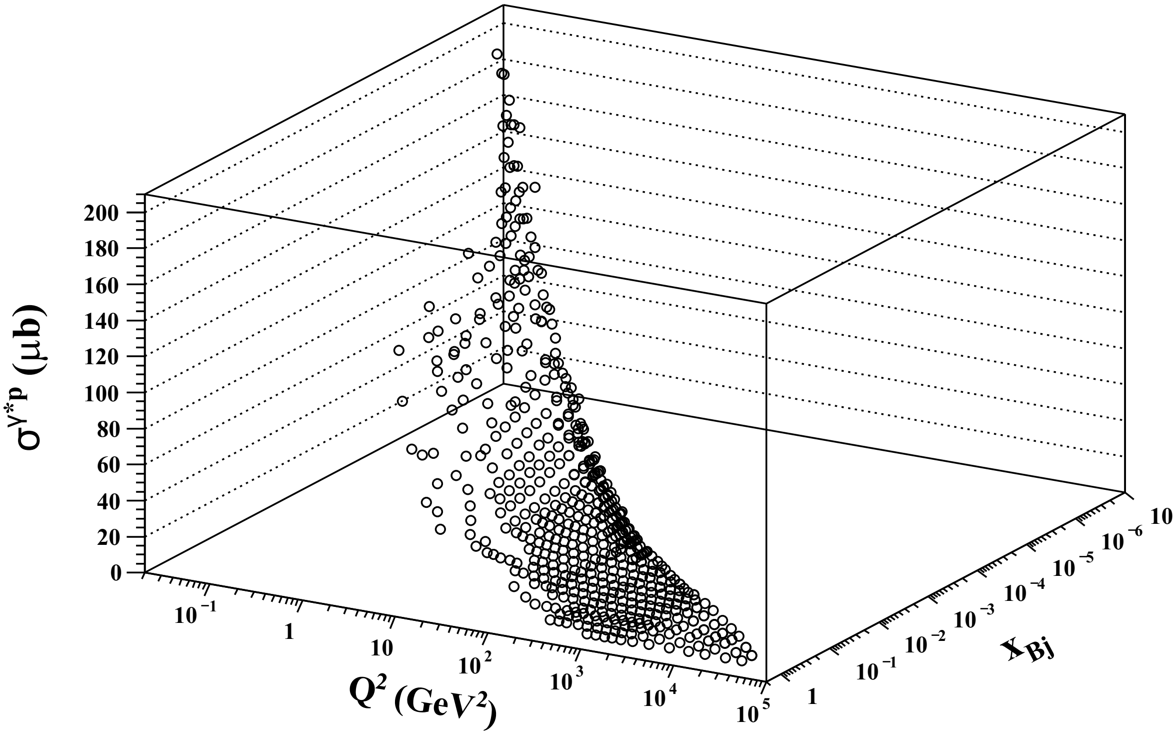

Figure 2: $\sigma^{\gamma^* p}(x_{\mathrm{Bj}}, Q^2)$ as extracted from the HERA e^+p NC data at $\sqrt{s} = 318$ and 300 GeV. For some values of Q^2 and x_{Bj}, two data points corresponding to the two different centre-of-mass energies are shown.

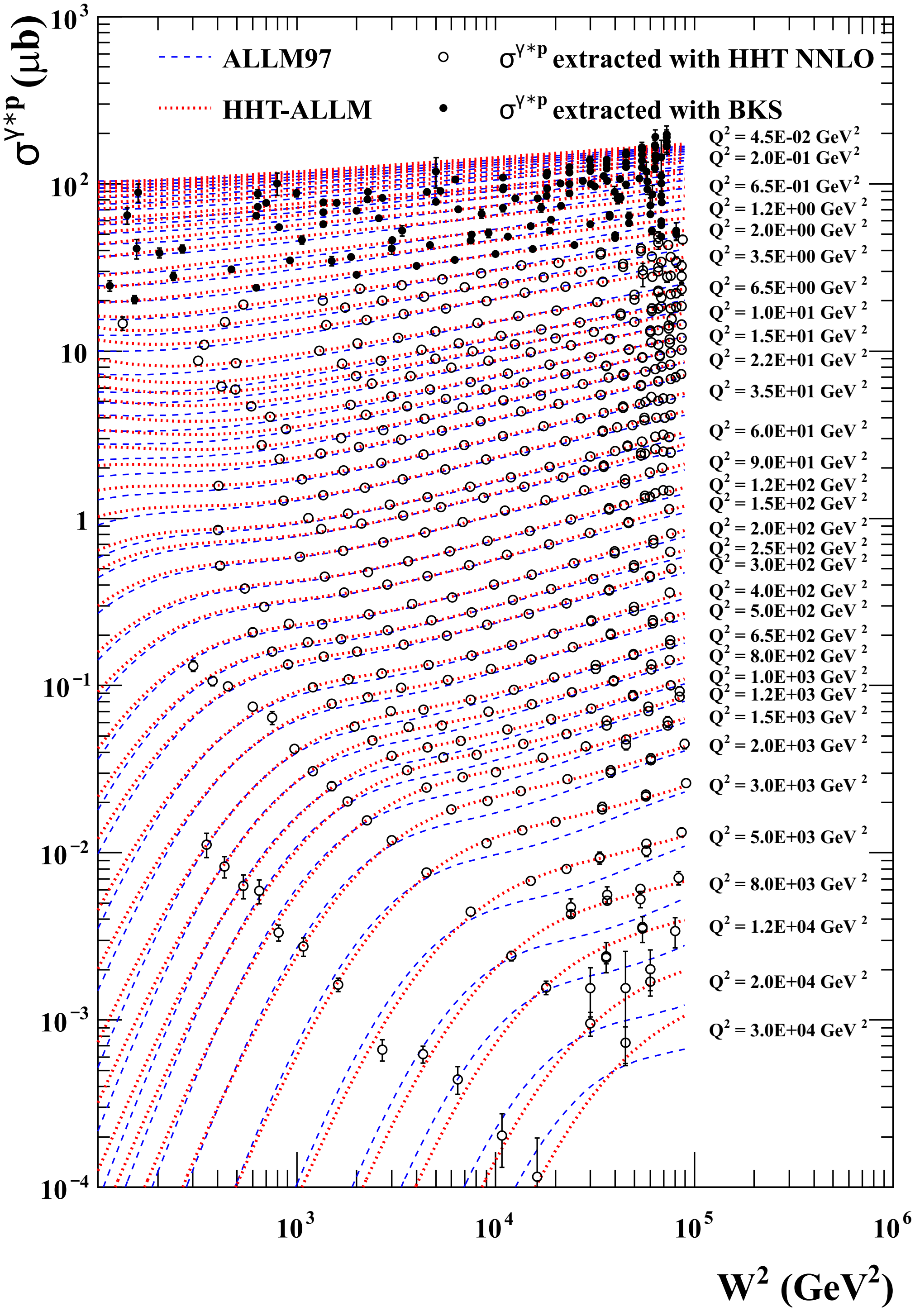

Figure 3: $\sigma^{\gamma^* p}(W^2)$ as extracted from the HERA e^+p NC data at $\sqrt{s}$ = 318 and 300 GeV. For some values of Q^2 and W, two data points corresponding to the two different centre-of-mass energies are shown. Also shown are the predictions from the ALLM97 fit to early HERA data and the result of the new HHT-ALLM fit, see text for details about the fit. Below Q^2 = 90 GeV^2, some Q^2 labels are omitted for reasons of legibility.

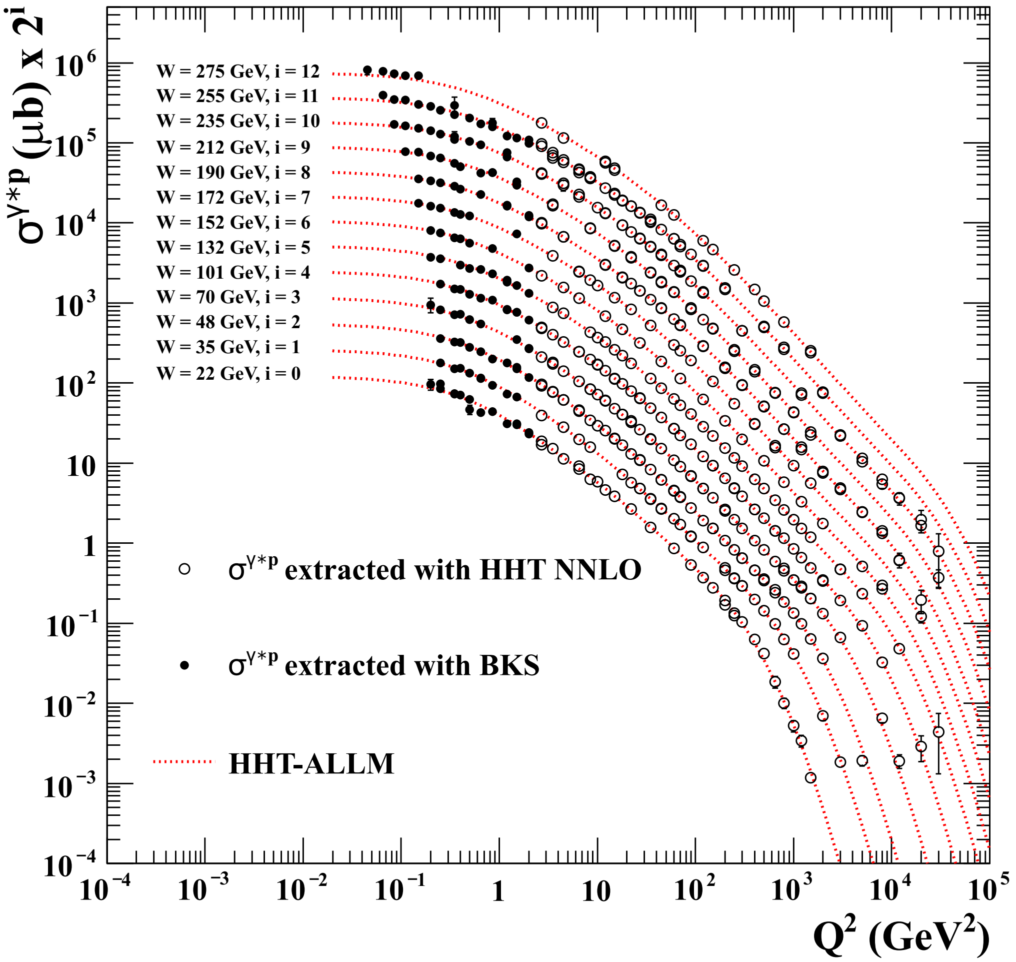

Figure 4: $\sigma^{\gamma^* p}(Q^2)$ as extracted from the HERA e^+p NC data at $\sqrt{s} = 318$ and 300 GeV for selected values of W, together with the predictions of the HHT-ALLM fit. For some values of Q^2 and W, two data points corresponding to the two different centre-of-mass energies are shown. The parameters from the HHT-ALLM fit were used to translate the data points to the W values listed. The values of $\sigma^{\gamma^* p}(Q^2)$ are multiplied by 2^i for different values of W to make the curves individually visible.

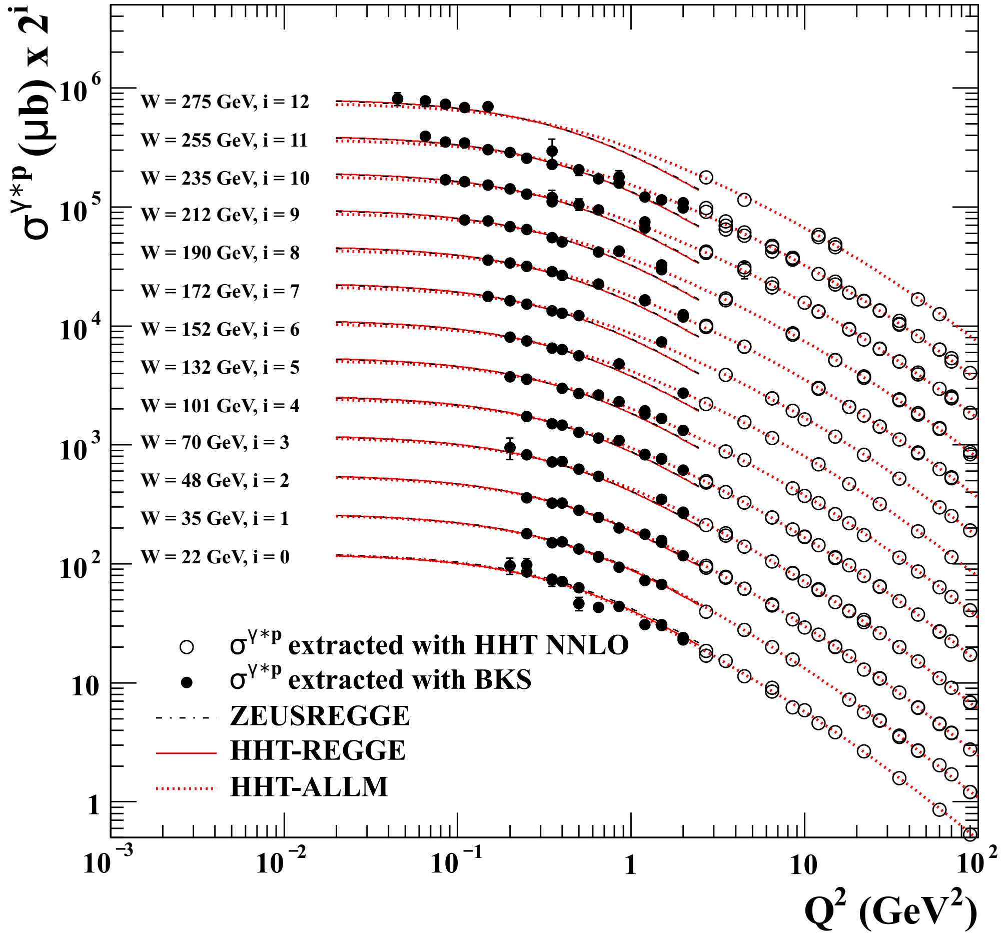

Figure 5: $\sigma^{\gamma^* p}(Q^2)$ in the low-Q^2 regime as extracted from the HERA e^+p NC data at $\sqrt{s}$ = 318 and 300 GeV for selected values of W, together with the predictions of the HHT-ALLM, HHT-REGGE and ZEUSREGGE fits, see text. The HHT-REGGE and ZEUSREGGE curves are almost identical. For some values of Q^2 and W, two data points corresponding to the two different centre-of-mass energies are shown. The parameters from the HHT-ALLM fit were used to translate the data points to the W values listed. The values of $\sigma^{\gamma^* p}(Q^2)$ are multiplied by 2^i for different values of W to make the curves individually visible.

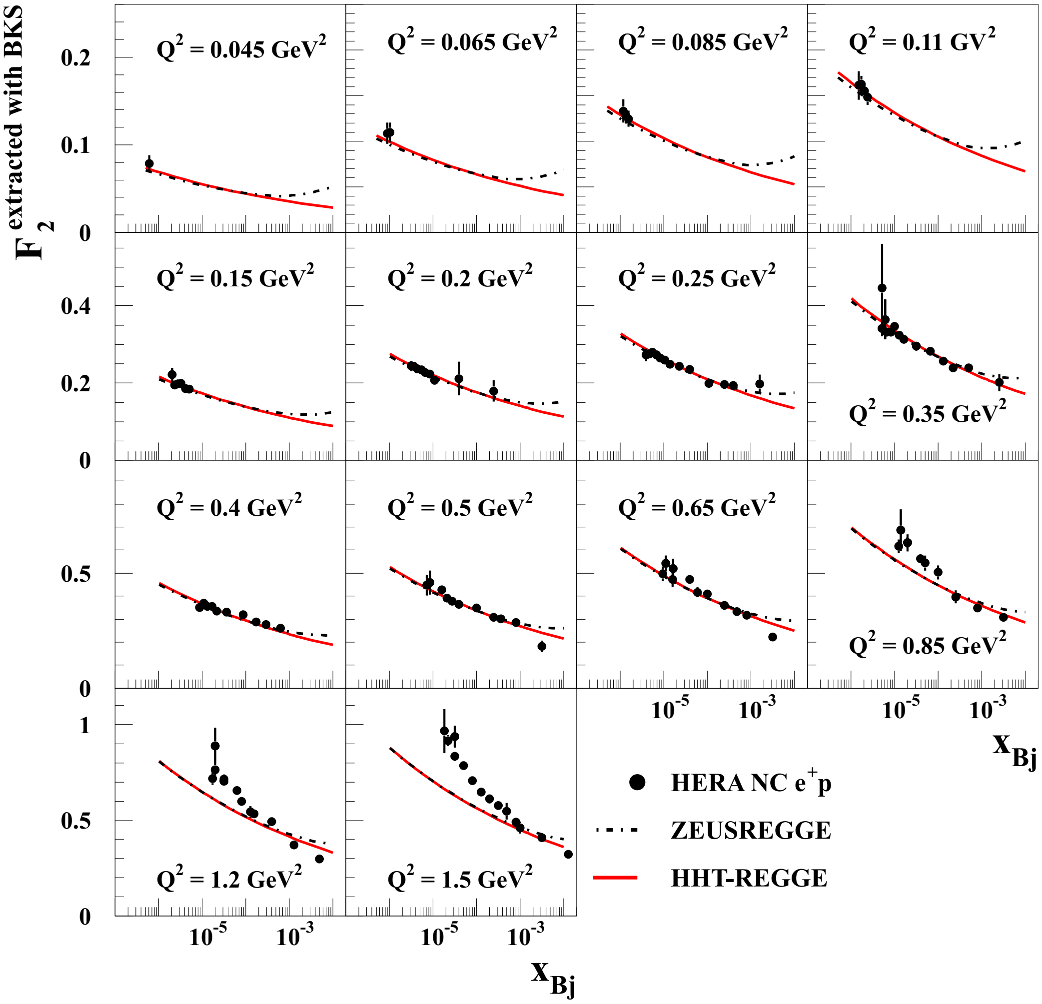

Figure 6: The structure-function F_2 as a function of x_{Bj} for low Q^2 as extracted from the HERA NC e^+p cross sections, together with predictions from the HHT-REGGE and ZEUSREGGE fits, see text for details.

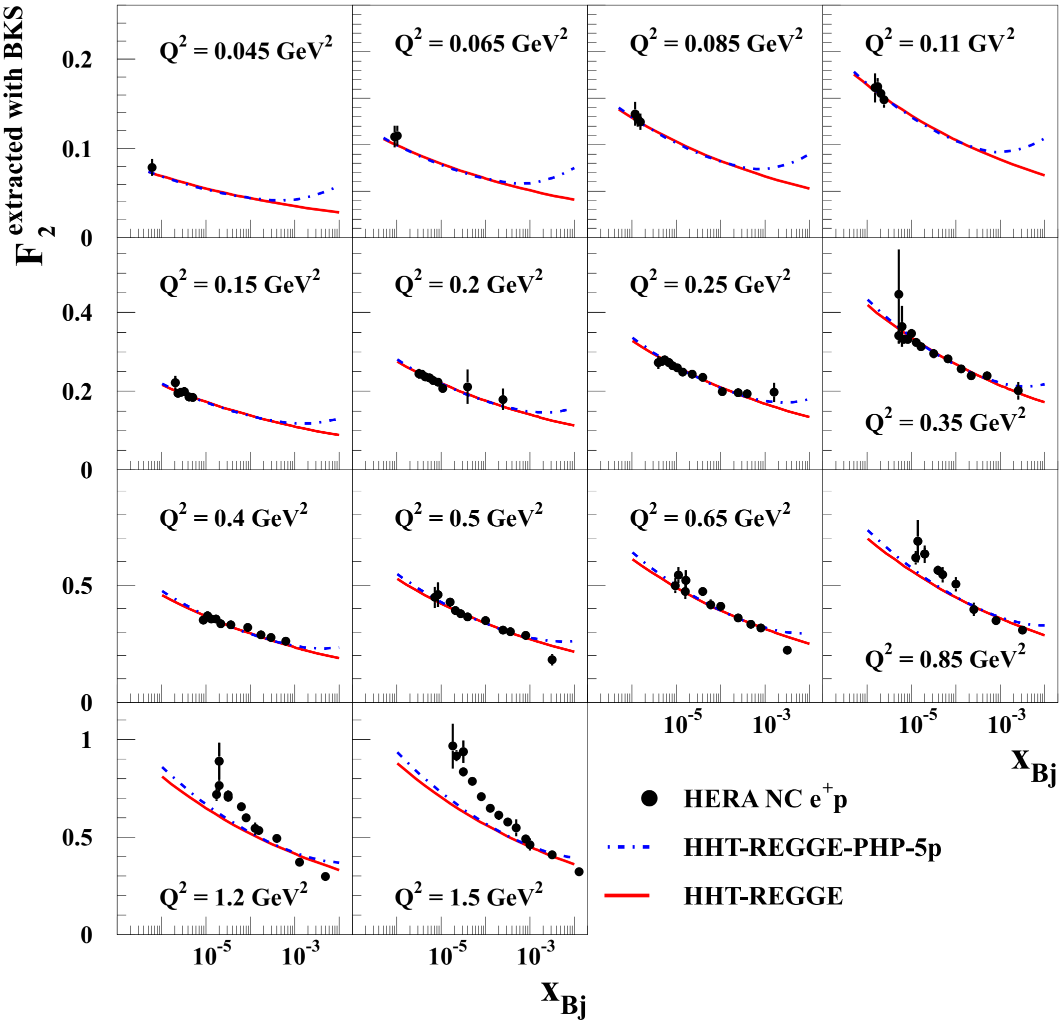

Figure 7: The structure-function F_2 as a function of $x_{\rm Bj}$ for low Q^2 as extracted from the HERA NC e^+p cross sections, together with predictions from the HHT-REGGE and HHT-REGGE-PHP-5p fits, see text for details.

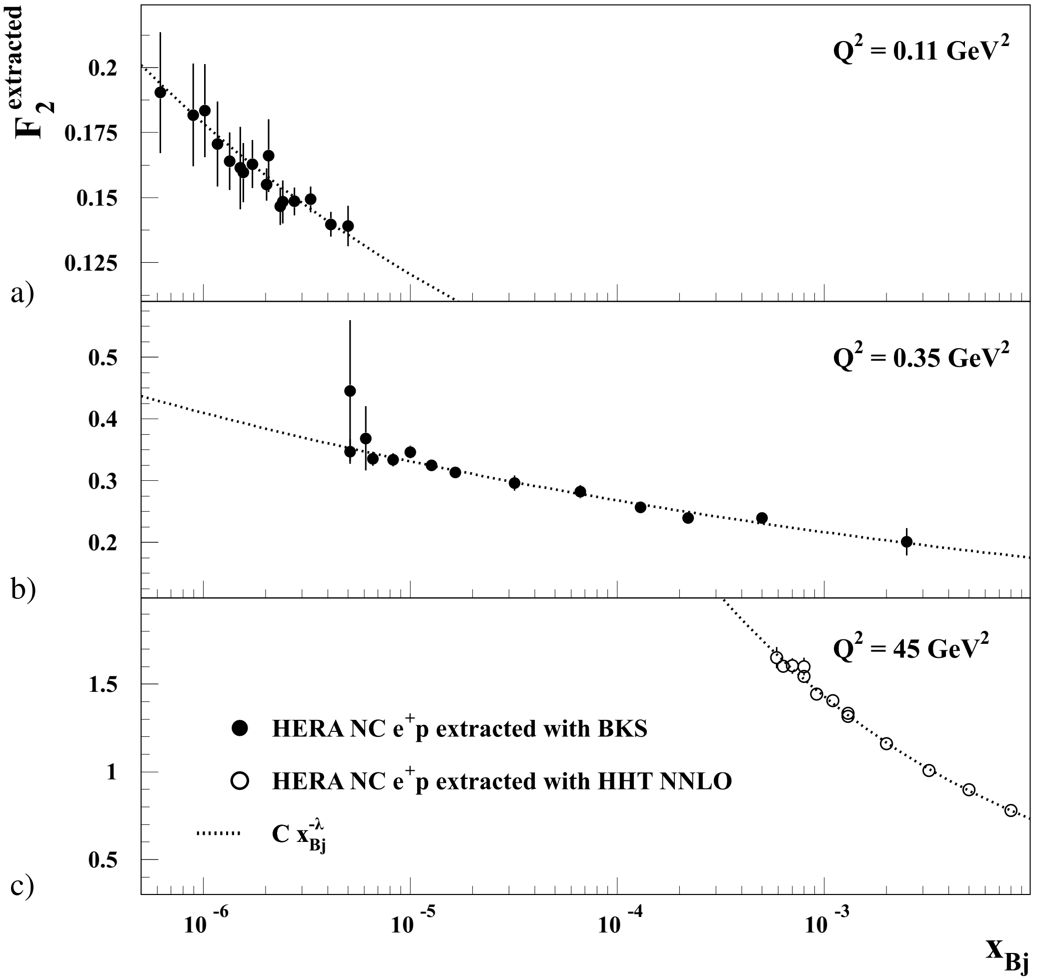

Figure 8: Values of F_2 extracted with the BKS model for a) $Q^2 = 0.11\,\mathrm{GeV}^2$, b) $Q^2 = 0.35\,\mathrm{GeV}^2$, and c) for $Q^2 = 45\,\mathrm{GeV}^2$ extracted within the framework of pQCD using the results of the HHT NNLO analysis. Also shown are fits according to $F_2 = C\, x_{\mathrm{Bj}}^{-\lambda}$.

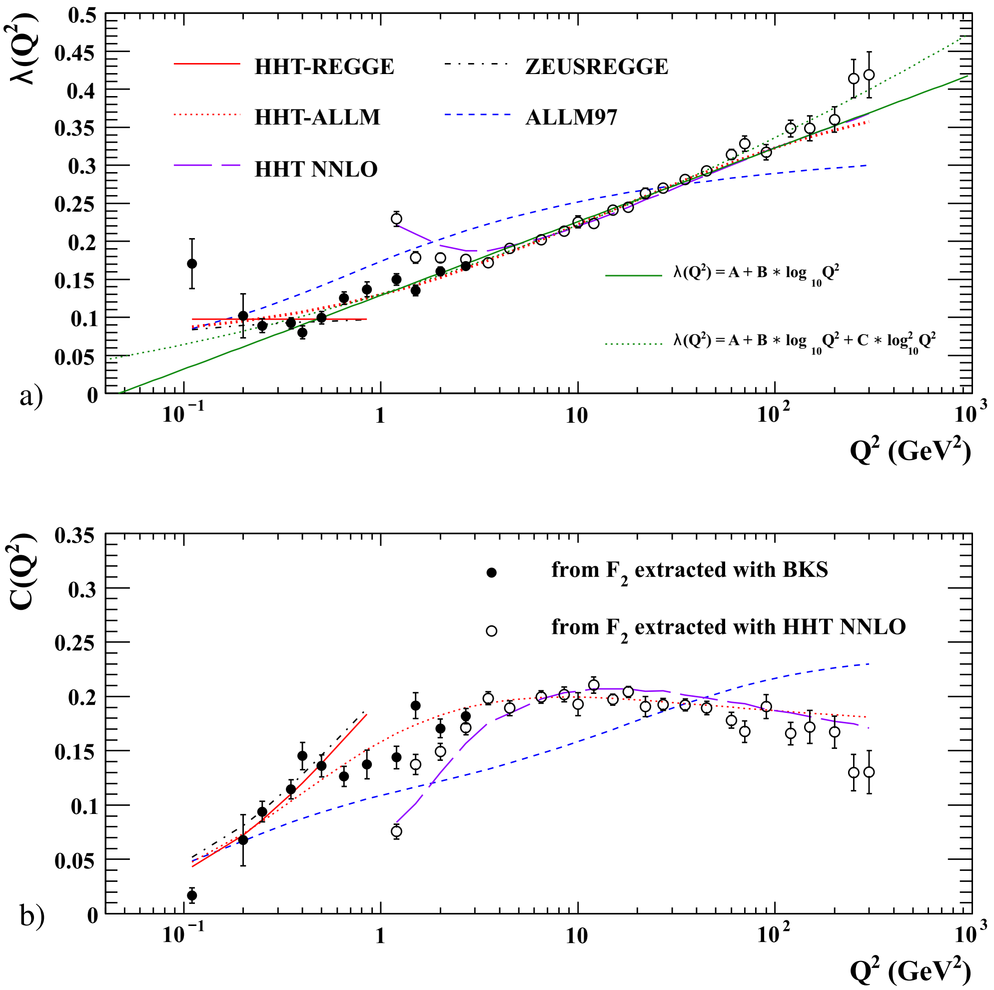

Figure 9: Values of a) λ and b) C determined in fits to $F_2(x_{\rm Bj}, Q^2) = C(Q^2)\, x_{\rm Bj}^{-\lambda(Q^2)}$, where F_2 was extracted either within the framework of pQCD using the results of the HHT NNLO analysis or with the BKS model, as appropriate. Also shown are predictions from HHT NNLO, HHT-ALLM, ALLM97, HHT-REGGE and ZEUSREGGE, for details see text, and fits to λ with a straight line and a quadratic function.

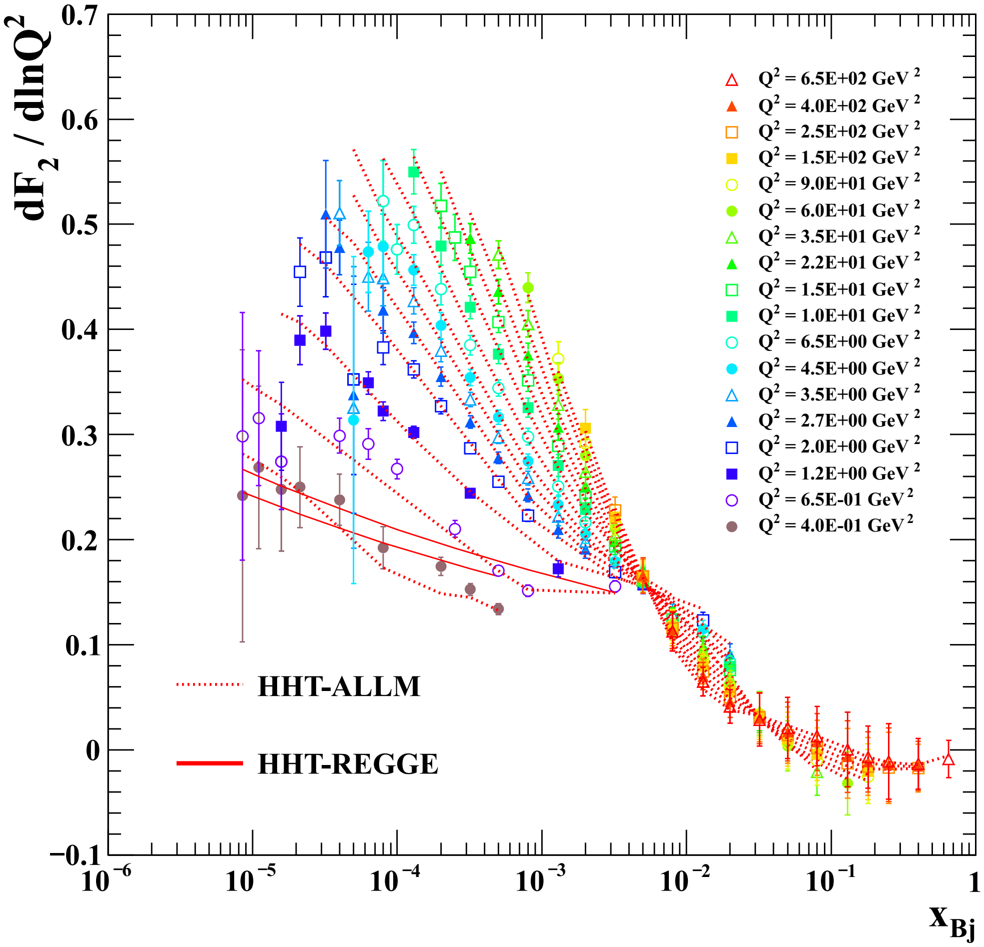

Figure 10: The derivative $dF_2/d\ln Q^2$ as a function of $x_{\rm Bj}$ for selected values of Q^2 over the full range in $x_{\rm Bj}$. Also shown are HHT-ALLM predictions (dotted lines) and HHT-REGGE predictions for $Q^2 = 0.4$ (lower solid line) and $Q^2 = 0.65\,\text{GeV}^2$ (upper solid line).

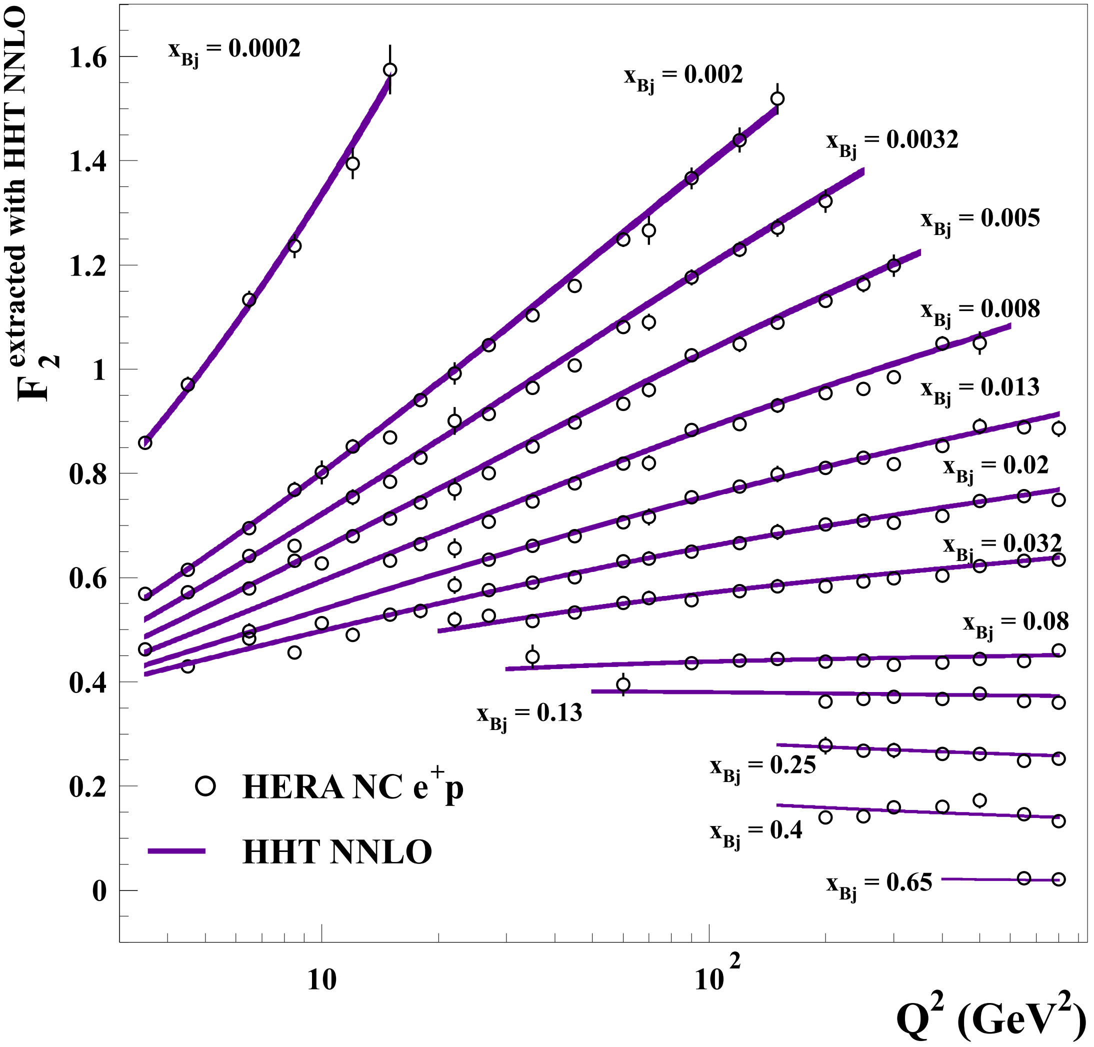

Figure 11: The structure-function $F_2(Q^2)$ for selected values of x_{Bj} in the Q^2-range where F_2 can be extracted within the framework of pQCD using the HHT NNLO analysis. Also shown are the predictions from HHT NNLO. The width of the bands represents the uncertainty on the predictions.

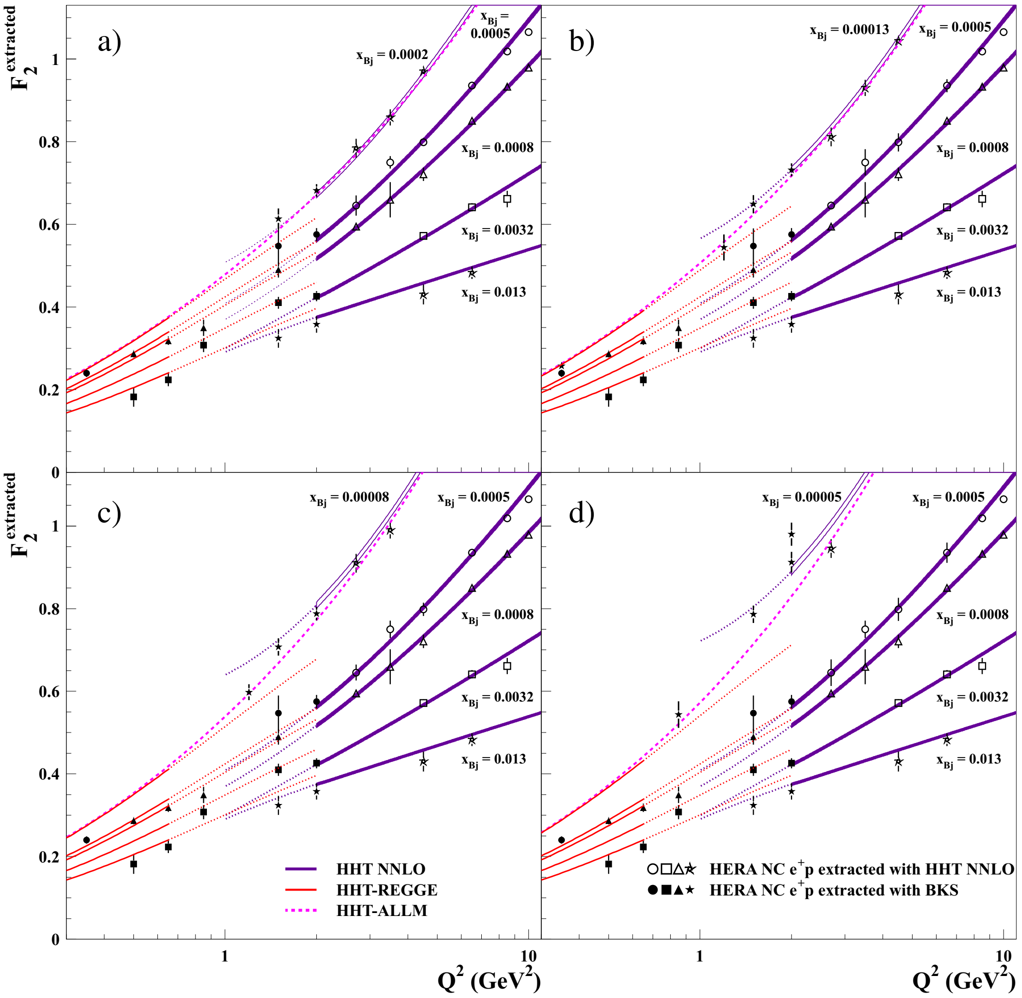

Figure 12: The structure-function $F_2(Q^2)$ for selected values of x_{Bj}, extracted with the BKS model for $Q^2 \leq 2\,\text{GeV}^2$ and with results from the HHT NNLO analysis for $Q^2 > 2\,\text{GeV}^2$. Each of the four plots contains data for four x_{Bj} values from 0.013 to $5 \cdot 10^{-4}$ and one additional x_{Bj} value, ranging from $x_{\text{Bj}} = 2 \cdot 10^{-4}$ in a) to $x_{\text{Bj}} = 5 \cdot 10^{-5}$ in d). Also shown are the predictions from the HHT-REGGE fit and the HHT NNLO analysis, together with the HHT-ALLM prediction. Dotted lines indicate extrapolations beyond the fitted regions. The width of the bands represents the uncertainty on the HHT NNLO predictions. No uncertainties were computed for the HHT-REGGE and HHT-ALLM predictions. For $x_{\text{Bj}} = 0.00005$ and $Q^2 = 2\,\text{GeV}^2$, two points are shown, extracted from data with $\sqrt{s} = 318$ and 300 GeV, respectively.

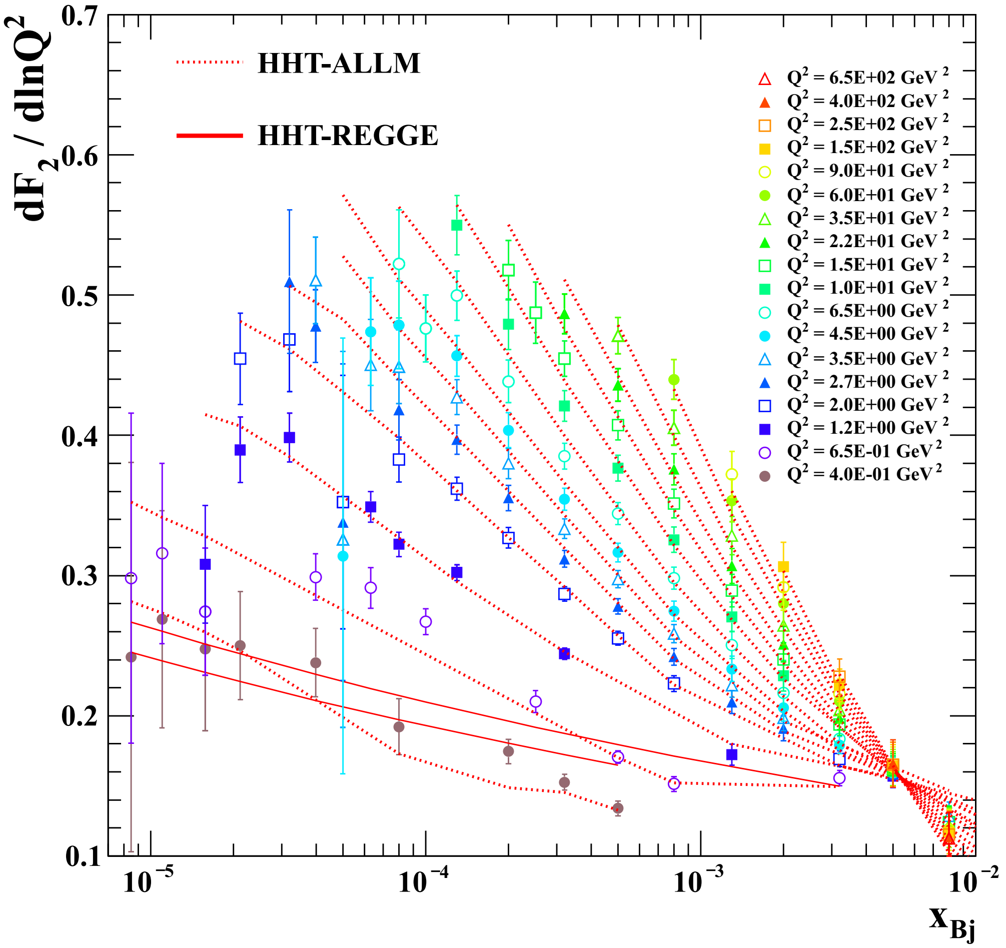

Figure 13: The derivative $dF_2/d\ln Q^2$ as a function of $x_{\rm Bj}$ for selected values of Q^2 for $x_{\rm Bj} < 10^{-2}$. Also shown are HHT-ALLM predictions (dotted lines) and HHT-REGGE predictions for $Q^2 = 0.4$ (lower solid line) and $Q^2 = 0.65\,{\rm GeV}^2$ (upper solid line).

Appendix

The ALLM parameterisation

The ALLM parameterisation is based on Regge phenomenology, but tries to incorporate ideas of pQCD. The parameterisation has 23 parameters [24] defined as follows:

$$
\begin{aligned}
F_2 &= \frac{Q^2}{Q^2 + m_0}\left(F_2^{I\!P} + F_2^{I\!R}\right) \\
F_2^{I\!P} &= c_{I\!P} * x_{I\!P}^{a_{I\!P}} (1 - x_{Bj})^{b_{I\!P}} \\
F_2^{I\!R} &= c_{I\!R} * x_{I\!R}^{a_{I\!R}} (1 - x_{Bj})^{b_{I\!R}} \\
\frac{1}{x_{I\!P}} &= 1 + \frac{W^2 - m_p^2}{Q^2 + p_1} \qquad \text{where } m_p \text{ is the proton mass} \\
\frac{1}{x_{I\!R}} &= 1 + \frac{W^2 - m_p^2}{Q^2 + p_2} \\
t &= \ln\left(\frac{\ln \frac{Q^2 + p_3}{p_4}}{\ln \frac{p_3}{p_4}}\right) \\
c_{I\!P} &= p_5 + (p_5 - p_6)\left[\frac{1}{1 + t^{p_7}} - 1\right] \\
a_{I\!P} &= p_8 + (p_8 - p_9)\left[\frac{1}{1 + t^{p_{10}}} - 1\right] \\
b_{I\!P} &= p_{11} + p_{12} t^{p_{13}} \\
c_{I\!R} &= p_{14} + p_{15} t^{p_{16}} \\
a_{I\!R} &= p_{17} + p_{18} t^{p_{19}} \\
b_{I\!R} &= p_{20} + p_{21} t^{p_{22}} \; .
\end{aligned}
$$

The parameters were determined in fits to the combined HERA e^+p NC cross sections, HHT-ALLM, and to the combined HERA data together with fixed-target data [25–27], HHT-ALLM-FT. They are listed in Table 8, where they are also compared to the parameters published previously [24].

As the HHT-ALLM fit describes the data well with a $\chi^2/\mathrm{ndf} = 1.06$, the parameters were used to translate data points to selected W or Q^2 values.